Title

Cellular Recruitment by Podocyte-Derived Pro-migratory Factors in Assembly of the Human Renal Filter

Authors

Kim, Albert D
Lake, Blue B
Chen, Song
et al.

Publication Date

2019-10-01

DOI

10.1016/j.isci.2019.09.029

Peer reviewed

iScience

CellPress

Article

Cellular Recruitment by Podocyte-Derived Pro-migratory Factors in Assembly of the Human Renal Filter

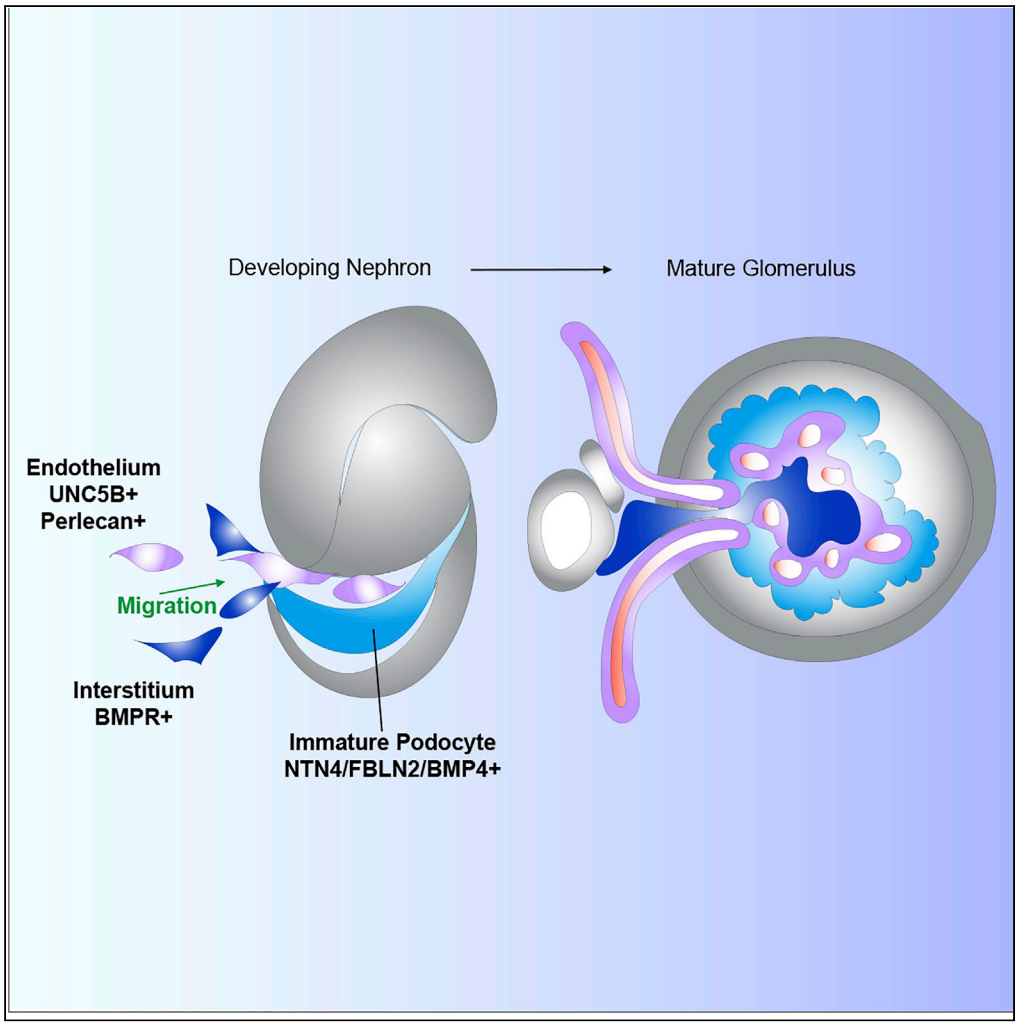

Albert D. Kim, Blue B. Lake, Song Chen, ..., Jill A. McMahon, Kun Zhang, Andrew P. McMahon

kzhang@bioeng.ucsd.edu (K.Z.)
amcmahon@med.usc.edu (A.P.M.)

HIGHLIGHTS

Single-nuclear RNA-seq analysis of human fetal kidney development

Co-ordinated programs of podocyte-driven glomerular development

Secreted podocyte factors act on endothelial and interstitial cells

DATA AND CODE AVAILABILITY

114569

Kim et al., iScience *20*, 402–414
October 25, 2019
https://doi.org/10.1016/j.isci.2019.09.029

iScience

CellPress

Article

Cellular Recruitment by Podocyte-Derived Pro-migratory Factors in Assembly of the Human Renal Filter

Albert D. Kim,[1,4] Blue B. Lake,[2,4] Song Chen,[2] Yan Wu,[2] Jinjin Guo,[1] Riana K. Parvez,[1] Tracy Tran,[1] Matthew E. Thornton,[3] Brendan Grubbs,[3] Jill A. McMahon,[1] Kun Zhang,[2,*] and Andrew P. McMahon[1,5,*]

SUMMARY

Analysis of kidney disease-causing genes and pathology resulting from systemic diseases highlight the importance of the kidney's filtering system, the renal corpuscles. To elucidate the developmental processes that establish the renal corpuscle, we performed single-nucleus droplet-based sequencing of the human fetal kidney. This enabled the identification of nephron, interstitial, and vascular cell types that together generate the renal corpuscles. Trajectory analysis identified transient developmental gene expression, predicting precursors or mature podocytes express FBLN2, BMP4, or NTN4, in conjunction with recruitment, differentiation, and modeling of vascular and mesangial cell types into a functional filter. *In vitro* studies provide evidence that these factors exhibit angiogenic or mesangial recruiting and inductive properties consistent with a key organizing role for podocyte precursors in kidney development. Together these studies define a spatiotemporal developmental program for the primary filtration unit of the human kidney and provide novel insights into cell interactions regulating co-assembly of constituent cell types.

INTRODUCTION

The kidney is essential for metabolic waste excretion, the homeostatic balance of tissue fluids (water, salt, and pH), blood pressure and cell composition, and bone development and metabolism. Filtration is performed within the renal corpuscles (RCs) by a highly structured cellular device. This comprises a convoluted fenestrated glomerular endothelium supported by mesangial myofibroblasts that releases a plasma filtrate that enters the nephron between slit diaphragms generated by the foot processes of tightly adherent podocytes. Establishment of the glomerular filter is initiated by a stereotypic recruitment of pioneering endothelial cells to the developing podocytes followed secondarily by interstitial cells into the glomerular cleft of Comma and S-Shaped bodies (CSBs and SSBs) and sequential capillary formation (Figures 1A and 1B). Podocytes support development and maintenance of the glomerular vasculature via VEGFA (Eremina et al., 2003; Sison et al., 2010), whereas endothelial-derived PDGF signals promote mesangial development (Bjarnegård et al., 2004; Lindahl et al., 1998) before RC maturation (Figure 1C) (Levéen et al., 1994; Soriano, 1994). Single gene mutations resulting in end-stage renal disease cluster in genes showing podocyte-enriched expression, highlighting the central role of podocytes in normal kidney function (Brenner et al., 1996; Zhong et al., 2017). Advances in pluripotent stem cell-derived kidney organoid systems support parallel efforts to mechanistically dissect human kidney development to gain new insights into developmental programs relevant to treating or modeling disease states or generating functional systems (Takasato et al., 2016; Morizane et al., 2015; Wilson and Humphreys, 2019; Taguchi and Nishinakamura, 2015; Combes et al., 2019). A human-focused understanding of kidney development will complement other mammalian model systems to maximize effective application, predict new disease relationships, and identify novel developmental mechanisms (Combes et al., 2019; Lindström et al., 2018a, 2018b, 2018c; Menon et al., 2018; Wu et al., 2018).

RESULTS

Single-Nucleus Interrogation of Human Fetal Kidney

To generate insights into RC formation, we applied snDrop-seq to transcriptionally profile nuclei isolated from human fetal kidneys (Figure 2A). Our group, and others, have captured single-nuclear transcriptomes from other challenging tissues including postmortem adult brain (Lake et al., 2016, 2018) resolving distinct cell types (Lake et al., 2017; Wu et al., 2019). The benefits of the nuclear approach are that cryopreserved

[1]Department of Stem Cell Biology and Regenerative Medicine, Broad-CIRM Center, Keck School of Medicine, University of Southern California, Los Angeles, CA 90089, USA

[2]Department of Bioengineering, University of California San Diego, La Jolla, CA 92093, USA

[3]Maternal Fetal Medicine Division, University of Southern California, Los Angeles, CA, USA

[4]These authors contributed equally

[5]Lead Contact

*Correspondence: kzhang@bioeng.ucsd.edu (K.Z.), amcmahon@med.usc.edu (A.P.M.)

https://doi.org/10.1016/j.isci.2019.09.029

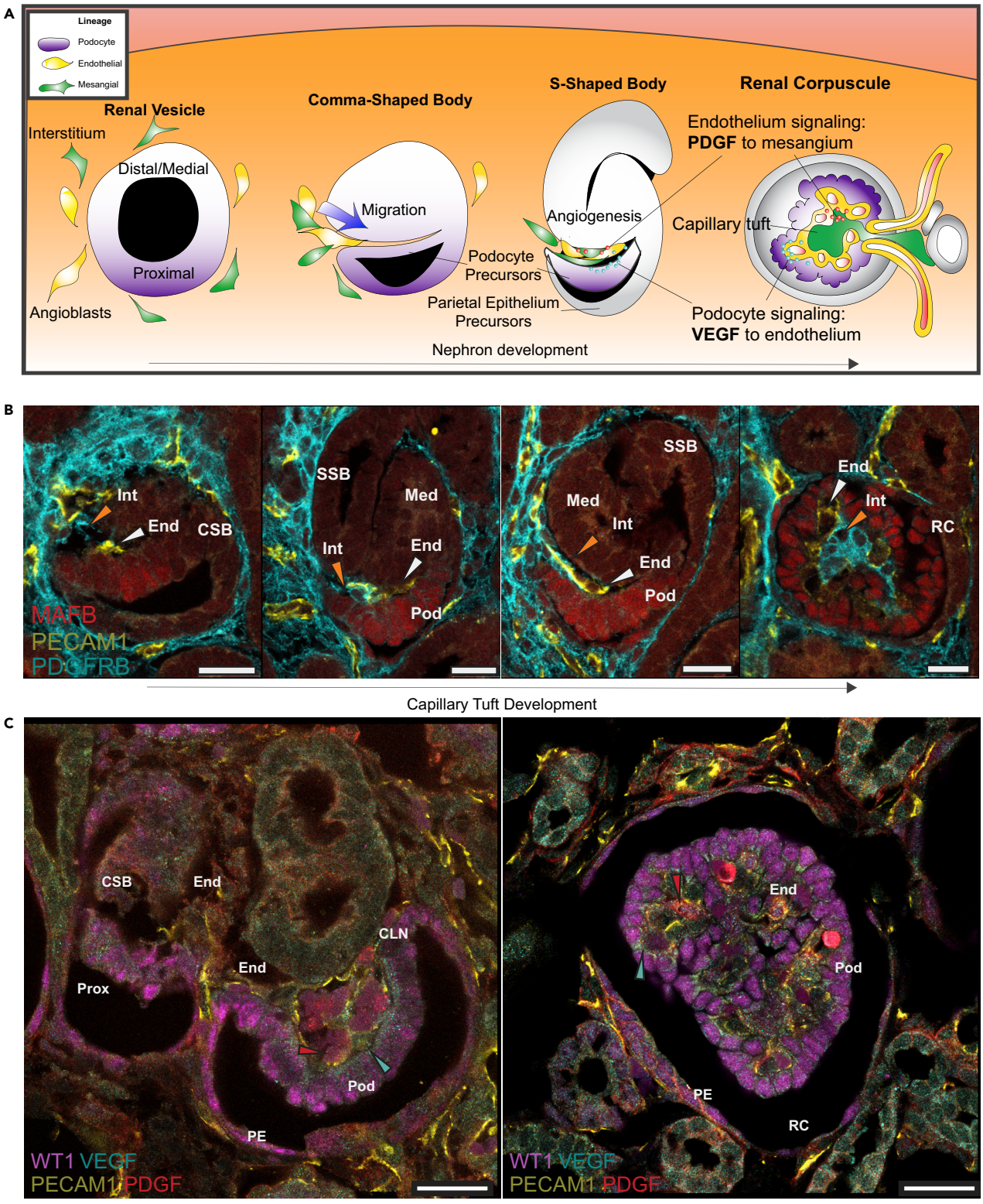

Figure 1. Schematic Model of RC Development

(A) Differentiating NPCs epithelialize to form a renal vesicle with distal/proximal polarity. Nephron morphogenesis progresses through CSB and SSB stages concomitant with the recruitment and invasion of mesenchymal endothelial and interstitial cells to the glomerular cleft, which is lined by developing

Figure 1. *Continued*

podocytes. Podocyte-derived VEGFA signaling to glomerular endothelial cells and PDGF secreted by endothelial cells acting on adjacent mesangial precursors are critical for the development, maintenance, and function of glomerular filtration.

(B) Immunostaining showing incremental stages of glomerular capillary tuft development starting with invasion of PECAM1+ endothelial cells (yellow) followed by PDGFRB + interstitial cells (cyan) into the glomerular cleft (left to right panels).

(C) Immunohistochemical staining of distinct stages of RC development labeling WT1+ PE, WT1+ podocytes colocalized with VEGFA (cyan arrowhead), and PECAM1+ endothelium colocalized with PDGF (red arrowhead).

(Scale bars, 25 μm). Prox, Proximal Nephron; Pod, Podocytes; PE, Parietal Epithelium; End, Endothelium; CSB, Comma-Shaped Body; CLN, Capillary Loop Nephron; RC, Renal Corpuscle.

tissue with potentially clinical value are compatible and epithelialized cells including those of sieved mature RCs are more accessible than by enzymatic cell dissociation methods required for whole cell. Podocytes are consistently under-represented (or missing) from prominent large kidney single cell RNA sequencing (RNA-seq) datasets (Adam et al., 2017; Park et al., 2018). Furthermore, our previous studies were unable to sufficiently access epithelialized cell types beyond SSB using an enzymatic cortical digestion method (Lindström et al., 2018a, 2018b, 2018d). To this end, we processed nephrogenic cortex and RCs from 13- to 16.5-week human fetal kidney samples that incorporated all stages of RC development to active filtering nephrons (Figures 2A and S1, Table S1). Nuclear RNA preferentially detects genes with high intron count compared with whole-cell RNA, leading to a systemic biased sensitivity toward genes that may escape detection in conventional single-cell approaches. Variable numbers of nuclei were obtained from each sample; whether the variation in number of nuclei reflects biological variability among the samples or technical variability in the procedures is not clear. Altogether, we generated data on 7,018 single nuclei from these combined samples sequenced to an average depth of 10,298 useful reads per nucleus (Table S1). This permitted detection of a median of 879 unique transcripts and 707 genes per nucleus, with genomic mapping rates showing the expected higher proportion of reads corresponding to intronic sequences (Table S1), as previously observed.

To resolve the cell type composition, we analyzed transcriptional heterogeneity by grouping cells by gene-gene covariance (see Transparent Methods). This approach identified twelve nephrogenic, five interstitial, one immune, and one endothelial cluster (Figure 2A and Tables S2 and S3). Clusters showed expression profiles and subgroup aggregations visualized with Uniform Manifold Approximation and Projection (UMAP) (Becht et al., 2018), independent of technical batch effects (Figures 2B, 2C, and S1). Cluster identification was supported by GO-Term analysis, immunohistological (protein-targeted) and *in situ* hybridization (mRNA-targeted) analysis with select known markers of mammalian kidney development, including LTBP1 (Schwab et al., 2006; Fetting et al., 2014), CDH4 (Dahl et al., 2002; Rosenberg et al., 1997), COL4A1 (Chen et al., 2016; Chew and Lennon, 2018), disease-related genes ESRRG (Berry et al., 2011; Harewood et al., 2010), PKHD1 (Igarashi and Somlo, 2002; Wilson, 2004), and novel marker PAMR1 (Figure S2, Tables S4 and S5). To visualize and infer relationships between clusters we employed similarity weighted non-negative embedding (SWNE) analysis (Figure 2D) (Wu et al., 2018b). Nephron progenitor cells (NPCs) and mitotic NPCs (cNPC) clusters were related to two differentiated NPC (dNPC) clusters enriched from cortex (Figure S1). Differentiated tubular clusters comprised medial/distal and proximal tubular identities (Figure 2D). DNPCs transitioned to parietal epithelium (PE), and podocyte clusters enriched in RC samples (Figures 2B and S1). Interstitial clusters were composed of interstitial progenitor cells (IPCs), mitotic interstitium (cINT), and three populations containing two mesangial clusters enriched in RC samples (INT1-3) (Figures 2B and S1).

Molecular Dissection of Podocyte Development

Given the nucleating role of the podocyte in the development of a glomerular filter we hypothesized that transiently expressed genes during podocyte development could be important coordinating glomerular and mesangial cell programs. An unsupervised pseudotemporal analysis in Monocle was used to identify intermediates in the podocyte developmental pathway (Figures 2C–2E, S3, and S4) (Qiu et al., 2017). Monocle analysis predicted that NPCs transitioned to dNPCs that expressed *PAX8*, *JAG1*, and *LHX1* (Park et al., 2007; Leimeister et al., 2003; Plachov et al., 1990) (Figures 2D–2G, Tables S6 and S7). *Lhx1* plays a key early role in mouse podocyte programs and mutations in LHX1 associated with congenital anomalies of the kidney and urinary tract (CAKUT) syndrome (Kobayashi et al., 2005; Boualia et al., 2013; Lindström et al., 2018d). Additionally, *JAG1* and *PAX8* are two markers of early nephron that are involved in kidney development and disease (Boualia et al., 2013; Narlis et al., 2007; Plachov et al., 1990; Lindström et al., 2018c; Liu et al., 2013; Chen and Al-Awqati, 2005; Piscione et al., 2004). DNPCs bifurcated between

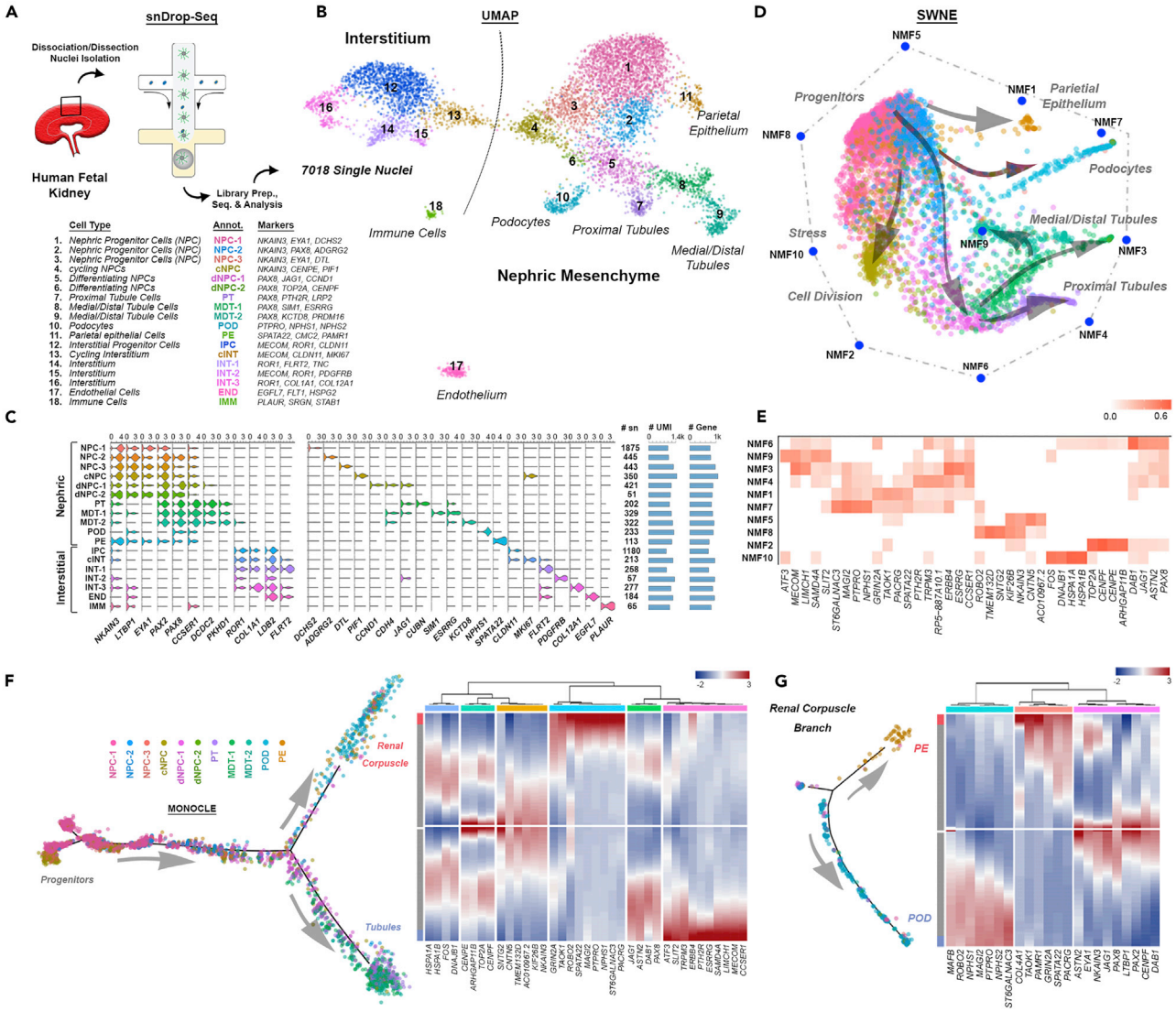

Figure 2. Single-Nucleus RNA Sequencing of the Developing Human Kidney and Pseudotemporal Ordering Resolves Major Cell Types and Informs on Podocyte Developmental Programs

(A) An overview of the snDrop-seq pipeline on fetal kidney samples (Table S1) including dissociated kidney cortical cells (14 and 16 weeks) and sieved glomeruli (13 and 15 weeks).

(B) Combined expression data (four individuals over five experiments) visualized by UMAP dimensional reduction showing 18 distinct cellular populations encompassing the nephrogenic, interstitial, endothelial, and immune cell types. Cell type annotations and associated select marker genes are indicated for each cluster.

(C) Violin plots showing expression values for select broad or cell-type specific marker genes. For each cluster, the number of datasets (SN), average number of transcripts (UMI), and average number of genes detected are indicated.

(D) SWNE visualization of nephrogenic lineage cell clusters and associated non-negative factorization (NMF) identified gene signatures indicate cluster relationships.

(E) Heatmap of top genes associated with each NMF state.

(F) Trajectory analysis using Monocle of nephrogenic lineages showing developmental progression into distinct RC (proximal) and tubule (medial/distal) lineages. Corresponding heatmap indicating discrete gene expression intensity from the progenitor state (gray center line value) maturing to either RC (red tip value) or medial/distal (blue tip value) branches.

(G) Trajectory analysis of the developing RC branch into either parietal or visceral (podocyte) epithelial cell types. Heatmap showing expression values of select marker genes progressing from differentiating NPCs (center, gray) to either parietal (red) or podocyte (blue) cell types.

See also Figures S1–S4.

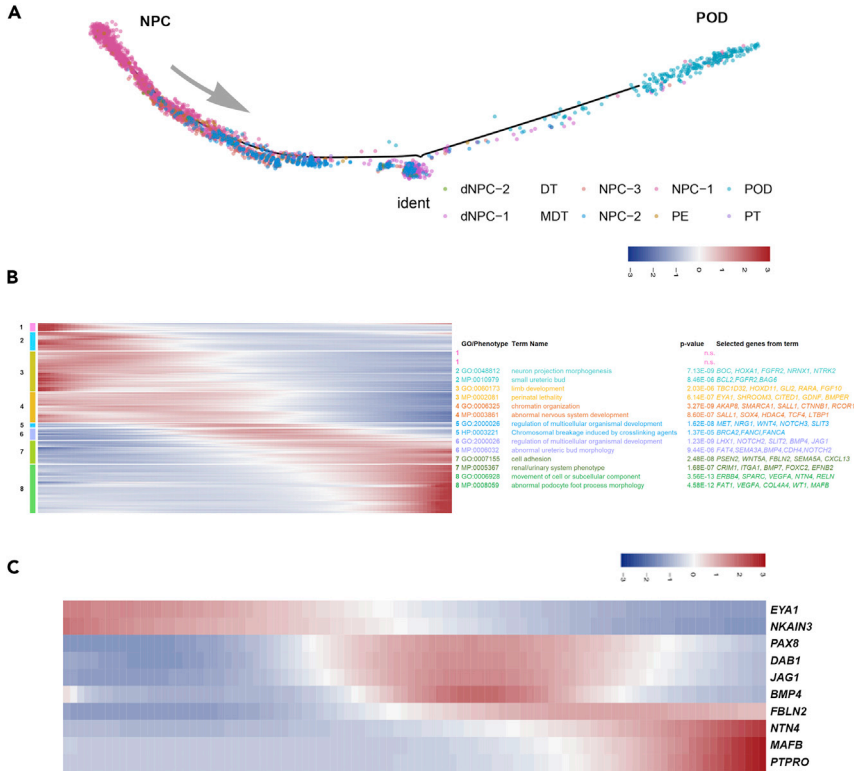

Figure 3. Trajectory Analysis of Podocyte Lineage Cells Identifies Distinct Transient Gene Expression Signatures

(A) Unidirectional trajectory of undifferentiated NPCs and podocyte lineage cells (see Transparent Methods) identified in Figure 2G.

(B) Identification of temporally significant stages of gene expression and their associated top gene ontology (GO) and mouse/human phenotype terms (select genes from each term are indicated). Cells are ordered according to the trajectory shown in (A).

(C) Heatmap of gene expression values for select stage-specific and expressed factors during podocyte development for cells ordered as in (A).

See also Figure S5.

medial/distal and proximal identities including podocytes (Figures 2F, S3, and S4, Table S6). Glomerulus-related GO Terms were associated with the proximal branch, whereas cytoskeletal processes were associated with the medial/distal branch (Tables S7–S11). Monocle analysis of proximal transcriptomes bifurcated podocyte and PE trajectories (Figures 2F, 2G, and S2E–S2E′). Global pseudotemporal analysis of this dataset identified eight temporally distinct gene sets (GS1–GS8) with distinct ontologies (Figures 3A and 3B, and Table S12). At one end, NPCs (GS1) expressed *ROBO2* and *ECEL* (Lindström et al., 2018b), whereas at the other end, mature podocytes (GS8) expressed *FOXC1, SYNPO, NPHS2* (Table S12), key genes in mouse and human podocyte function (Lindström et al., 2018a, 2018b; Motojima et al., 2017; Roselli et al., 2004; Yanagida-Asanuma et al., 2007; Mundel et al., 1997; Komaki et al., 2013; Kume et al., 2000; Franceschini et al., 2006; Sharif and Barua, 2018). GS6–GS8 gene-associated phenotypes included defects in ureteric bud, renal system, and podocyte foot processes accompanied with GO Terms for regulation of development, cell adhesion, and cell movement (Figure 3B and Table S12).

Examining these data for podocyte-derived, stage-specific developmental signals as potential organizers of the glomerular filter identified three expressed factors predicted to display partial temporal overlap: *BMP4* (GS6; a member of the BMP subfamily of TGFβ signals) (Padgett et al., 1993), *FBLN2* (GS7; a calcium-binding extracellular matrix protein of the fibulin family) (Zhang et al., 1994), and *NTN4* (GS8; a Netrin family member) (Figure 3C) (Yin et al., 2000). *In situ* hybridization demonstrated each exhibited expression in podocytes (but also other cell types) surrounding the glomerular cleft in conjunction with angioblast recruitment, although their spatiotemporal profiles differed (Figure 4A). In particular, *FBLN2* was detected at high levels in the earliest podocyte precursors, continued throughout RC development, but terminated

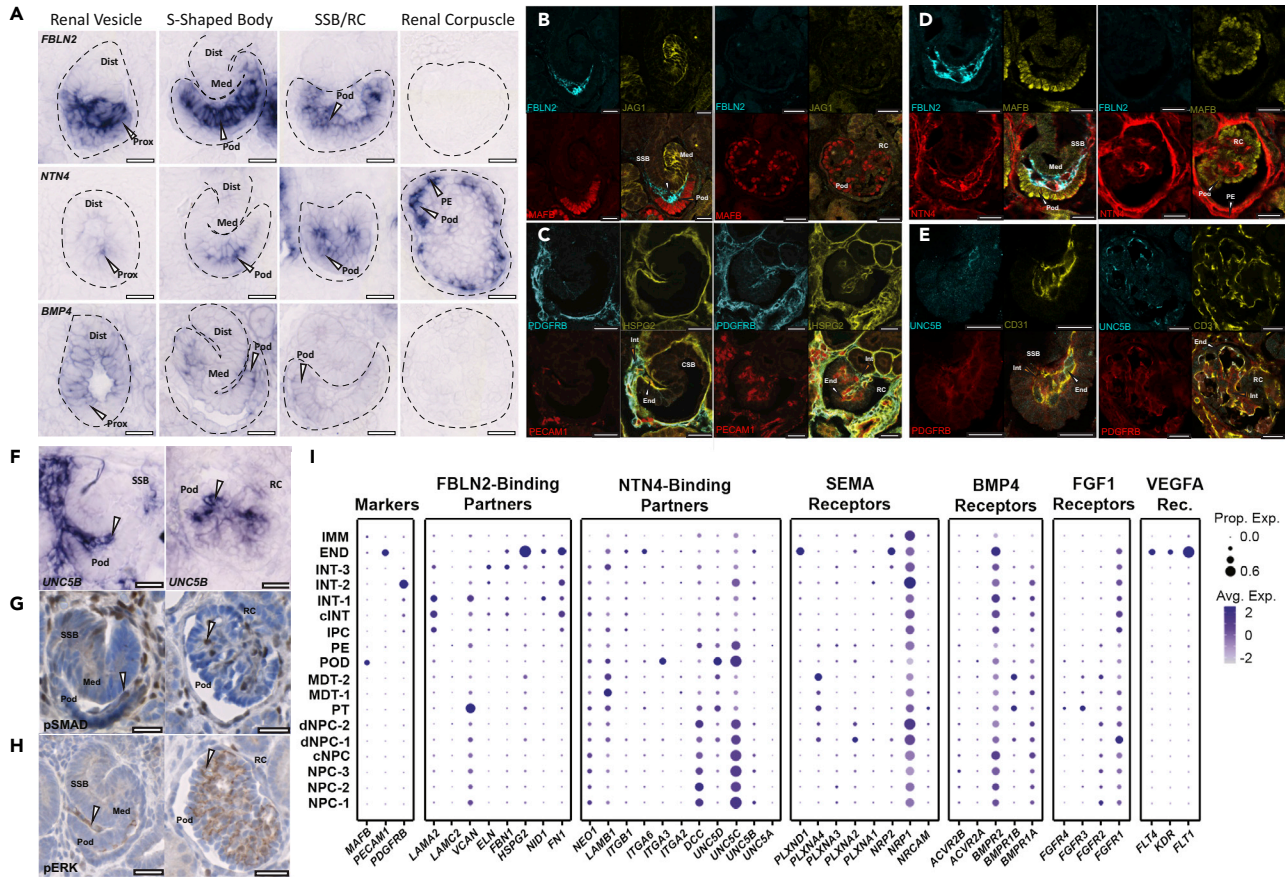

Figure 4. Spatiotemporal Mapping of the Expression of Genes Encoding Podocyte-Expressed Factors and Predicted Endothelial and Interstitial Cell Interactions

(A–E) (A) *In situ* hybridization for *FBLN2, NTN4,* and *BMP4* indicating gene expression (arrowheads) during intermediate phases of proximal fate to podocyte development. Arrowheads point to expression in developing podocytes that is absent in mature RCs, with the exception of NTN4, which is expressed in periglomerular vasculature and at lower levels in mature podocytes. Immunostaining in SSB and RC for (B) FBLN2, (C) HSPG2, (D) NTN4, (E) UNC5B, and indicated markers.

(F–H) (F) *In situ* hybridization of *UNC5B*. Phospho-SMAD1/5- (G) and phospho-ERK- (H) positive cells (arrowheads) showing labeling of infiltrating cells into the glomerular cleft in SSB and in RCs (scale bars, 25 μm). Dist, Distal Nephron; Med, Medial Nephron; Prox, Proximal Nephron; Pod, Podocytes; PE, Parietal Epithelium; SSB, S-Shaped Body; RC, Renal Corpuscle.

(I) Dot pots showing relative expression (blue color intensity) and relative number of positive nuclei (dot size) for extracellular matrix and cell signaling genes found within clusters identified in Figure 1A.

See also Figure S5.

in the functional RC (Figure 4A). FBLN2 was detected within the glomerular cleft and angioblasts produced PERLECAN/HSPG2, a potential interaction partner for FBLN2(Brown et al., 1997) (Figures 4B and 4C). UNC5B, a surface receptor for NTN4 known to be involved in diabetic nephropathy (Lu et al., 2004; Hoang et al., 2009; Lejmi et al., 2014; Ranganathan et al., 2015; Wang et al., 2008), was also detected on the angioblast (Figures 4D and 4E), continuing into periglomerular endothelial cells of mature RCs, and on parietal epithelial cells that encapsulated the RC (Figures 4D and 4F). Analysis of phospho-SMAD and ERK staining, respectively, suggests evidence including but not limited to potential activation of BMP and FGF signaling within the vascular/mesangial population invading the glomerular cleft (Figures 4G and 4H). These data support potential roles for FBLN2, NTN4, and BMP4 in RC assembly from the initial stages of endothelial and interstitial recruitment (Figure 4I).

Endothelial and Interstitial Cell Responses to Podocyte-Derived Expressed Factors

NTN4 and BMP4 are known to have multiple roles in kidney and glomerular disease and development (Dudley et al., 1999; Michos et al., 2007; Miyazaki et al., 2000; Oxburgh et al., 2005, 2011;

Raatikainen-Ahokas et al., 2000; Ueda et al., 2008; Wang et al., 2008), and non-glomerular associated Fbln2 expression has been reported in the mouse kidney (Pan et al., 1993); however, no specific role has been attached to any of these factors in coordinating glomerular endothelial or mesangial programs in the human kidney. To explore the function of these factors on human vascular and mesangial cell development, biologically relevant primary endothelial and interstitial cell types were isolated from the human fetal kidney by enzymatic dissociation of the cortical region and antibody specific enrichment (anti-VECAD1, endothelial; anti-PDGFRB, interstitial) (Figure 5A) and tested for high-affinity responses to nanomolar concentrations of specific factors informed by the previous literature. As expected from published studies (Barkefors et al., 2008), VEGFA promoted endothelial cell migration through a cell permeable membrane, reflecting *VEGFA*'s known actions in facilitating early assembly of the glomerular vasculature (Figure 1), increased angiogenic tubule formation in Matrigel (Figures 5B and 5C), and enhanced endothelial cell proliferation (Figure S5B). Interestingly, FBLN2 and NTN4 but not BMP4 also increased endothelial cell migration and angiogenic tube formation but did not alter proliferation suggesting a partial overlap with VEGFA-stimulated activities (Figures 5B–5E, S5A, and S5B). NTN4 has been shown to elicit context-dependent angiogenic or anti-angiogenic responses consistent with observations here (Lambert et al., 2012; Nacht et al., 2009; Hoang et al., 2009). FBLN2 has been linked to cell adhesion (Pfaff et al., 1995), and the transient accumulation in the matrix surrounding migrating endothelial cells in the glomerular cleft is consistent with matrix interactions promoting adhesion and cell spreading (Figures 4B, 4D, and S5C). To examine FBLN2 action further, a scratch assay was performed on a confluent population of endothelial cells to determine if FBLN2 influences cell spreading at the leading edge, a sensitive and quantitative assay of general cell motility and cytoskeletal spreading in a homogeneous environment that was previously described (Yarrow et al., 2004). A marked increase in lamellar extensions was observed in the presence of FBLN2 and this response was abrogated by co-incubation with Endorepellin, an inhibitory subunit of HSPG2 that is thought to inhibit FBLN2-HSPG2 interactions and is generally anti-angiogenic (Poluzzi et al., 2016; Mongiat et al., 2003; Brown et al., 1997; Douglass et al., 2015) (Figures 5F and 5G). Additionally, endothelial cells preferentially adhered to an FBLN2-coated surface, an interaction that was strongly inhibited on addition of Endorepellin (Figures 5H and 5I). Together these support a role for podocyte-expressed FBLN2 acting at least in part through endothelial-produced HSPG2 in promoting outgrowth, migration, and adhesion of endothelial cells in glomerular morphogenesis. Interestingly, mouse Fbln2 does not show similar dynamic podocyte restricted activity in RC development and is instead restricted to the apical domain of tubular epithelia (Figure S5D). A closely related gene Fbln1 is expressed in the glomerular cleft in mouse but is widely detected, whereas FBLN1 is nearly absent in human kidney tissues suggesting a marked species difference in the regulation of both genes with respect to podocyte development (Figure S5D). Although VEGFA, FBLN2, and NTN4 may all act together at early stages of glomerular morphogenesis, only VEGFA and NTN4 are likely to play a continuing role in the maintenance of the glomerular network.

Podocyte-directed actions on the interstitial to mesangial cell transition are not well understood. Genetic studies in the mouse have shown endothelial cell-derived *PDGFB* acts through mesangial cell *PDGFRB* to promote mesangial cell-dependent formation of the glomerulus (Bjarnegård et al., 2004). PDGF pathway action plays a broader role in regulating pericytes, a myofibroblast-like cell type interacting with non-glomerular vasculature, which shares a common origin from interstitial progenitor cells (Kobayashi et al., 2014). To initially determine if PDGFRB + cortical interstitial cells show expected responses *in vitro*, we examined the effects of PDGFB. PDGFB addition enhanced interstitial cell migration across a cell permeable membrane (Figures 5B and 5C), and the proliferative stimulus invoked by PDGFB was inhibited by DMPQ (Lo et al., 2017), a specific PDGFRB inhibitor (Figures S5A and S5B). Thus, the *in vitro* system replicated PDGF/PDGFRB interactions. Interestingly, interstitial cells were also stimulated to migrate by FBLN2 similarly to endothelial cells by a yet unclear mechanism (Figure 5C). Interstitial trajectory analysis showed that interstitial progenitor cells generate different interstitial cell types (INT-1/INT-2/INT-3). In conjunction with the developmental progression, differential gene expression analysis predicted an upregulation of the BMP receptor *BMPR1B* and the transcriptional regulatory factor *GATA3,* involved in mesangial differentiation (Labastie et al., 1995) in INT-1/INT-2 cells (Figure 4H and Table S13), and an upregulation of BMP signaling inhibitors in INT-3 cells, a yet uncharacterized interstitial cell type (Tables S14 and S15). Both gain and loss of function of *Bmp4* in mouse podocytes result in glomerular capillary defects suggesting that precise regulation of BMP signaling is critical in RC programs (Ueda et al., 2008).

Consistent with a role for BMP signaling in human glomerular development, cells in the glomerular cleft exhibited phospho-SMAD1/5 activity (Figures 5J and S5F). Linked nuclear GATA3 raised the possibility

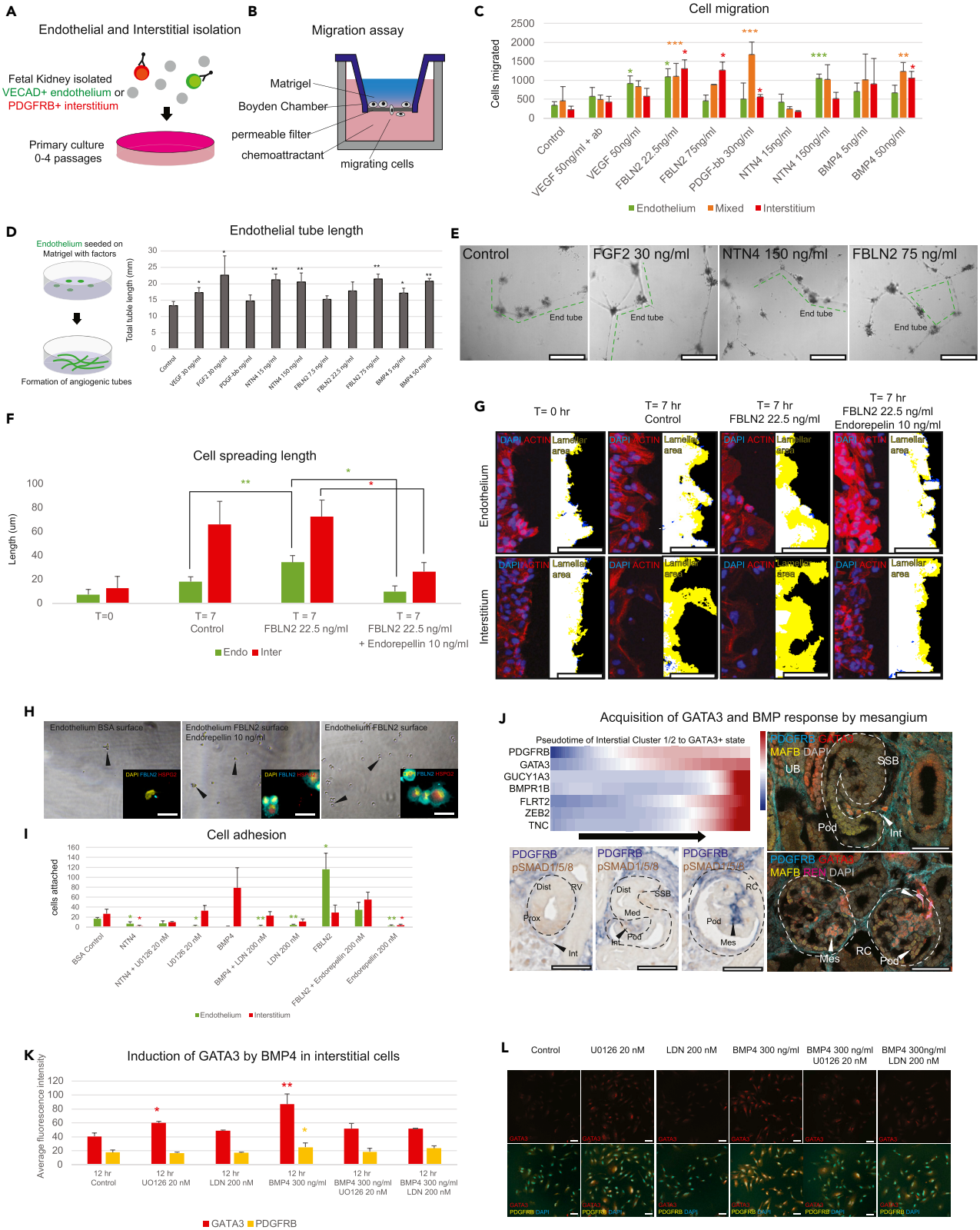
A
Endothelial and Interstitial isolation
Fetal Kidney isolated
VECAD+ endothelium or
PDGFRB+ interstitium
Primary culture
0-4 passages
B
Migration assay
Matrigel
Boyden Chamber
permeable filter
chemoattractant
migrating cells
C
Cell migration
Cells migrated
Control
VEGF 50ng/ml + ab
VEGF 50ng/ml
FBLN2 22.5ng/ml
FBLN2 75ng/ml
PDGF-bb 30ng/ml
NTN4 15ng/ml
NTN4 150ng/ml
BMP4 5ng/ml
BMP4 50ng/ml
Endothelium
Mixed
Interstitium
D
Endothelium seeded on
Matrigel with factors
Formation of angiogenic tubes
Endothelial tube length
Total tuble length (mm)
E
Control
FGF2 30 ng/ml
NTN4 150 ng/ml
FBLN2 75 ng/ml
End tube
F
Cell spreading length
Length (um)
T=0
T= 7
Control
T = 7
FBLN2 22.5 ng/ml
T = 7
FBLN2 22.5 ng/ml
+ Endorepellin 10 ng/ml
Endo
Inter
G
T= 0 hr
T= 7 hr
Control
T= 7 hr
FBLN2 22.5 ng/ml
T= 7 hr
FBLN2 22.5 ng/ml
Endorepelin 10 ng/ml
Endothelium
Interstitium
DAPI ACTIN
Lamellar area
H
Endothelium BSA surface
Endothelium FBLN2 surface
Endorepellin 10 ng/ml
Endothelium FBLN2 surface
I
Cell adhesion
cells attached
BSA Control
NTN4
NTN4 + U0126 20 nM
U0126 20 nM
BMP4
BMP4 + LDN 200 nM
LDN 200 nM
FBLN2
FBLN2 + Endorepellin 200 nM
Endorepellin 200 nM
Endothelium
Interstitium
J
Acquisition of GATA3 and BMP response by mesangium
Pseudotime of Interstial Cluster 1/2 to GATA3+ state
PDGFRB
GATA3
GUCY1A3
BMPR1B
FLRT2
ZEB2
TNC
PDGFRB GATA3
MAFB DAPI
UB
SSB
Pod
Int
PDGFRB
pSMAD1/5/8
Dist
RV
Prox
Int
Med
RC
Mes
PDGFRB GATA3
MAFB REN DAPI
K
Induction of GATA3 by BMP4 in interstitial cells
Average fluorescence intensity
12 hr
Control
12 hr
UO126 20 nM
12 hr
LDN 200 nM
12 hr
BMP4 300 ng/ml
12 hr
BMP4 300 ng/ml
UO126 20 nM
12 hr
BMP4 300 ng/ml
LDN 200 nM
GATA3
PDGFRB
L
Control
U0126 20 nM
LDN 200 nM
BMP4 300 ng/ml
BMP4 300 ng/ml
U0126 20 nM
BMP4 300ng/ml
LDN 200 nM
GATA3
PDGFRB DAPI

Figure 5. Chemotactic, Angiogenic, and Mesangial-Inductive Effects of FBLN2, NTN4, and BMP4

(A) Isolation of primary HFK endothelial and interstitial cells, subculture.

(B) Schematic of migration assay indicating input cells migrating through permeable filter to chemoattracting factor in the lower chamber.

(C) Quantitation of endothelial, interstitial, or mixed migration across permeable membrane in response to factors indicated.

(D–G) (D) Schematic and quantification of endothelial tube assay in response to factors indicated with (E) representative images of tube formation and dotted line highlighting tubes. Scale bars, 0.5 mm. (F) Quantification and (G) representative images of endothelial or interstitial cell lamellar extension length and area (yellow) in response and to factors indicated (scale bars, 50 μm).

(H and I) (H) Representative images and (I) quantitation of endothelial cell adhesion to surfaces coated with factors indicated (scale bars, 20 μm).

(J) Pseudotemporal upregulation of indicated genes during Interstitial cluster INT1/2 differentiation. Immunohistochemical staining of phospho-SMAD1/5 and PDGFRB costaining in renal vesicles, S-Shaped Bodies, and RCs showing colocalization in mesangial cells. Immunofluorescent staining of PDGFRB, GATA3, MAFB, and REN showing PDGFRB+/GATA3+ interstitial cells recruited to SSBs. REN + cells identify juxtaglomerular cells (Scale bars, 50 μm).

(K and L) (K) Quantification and (L) representative images of BMP4 induction of GATA3 and PDGFRB with or without the presence of pSMAD or MAPK inhibition of interstitial cells after 12 h (scale bars, 25 μm).

Data are represented as mean ± SEM. One asterisk (*) indicates p value smaller than 0.05 ($p < 0.05$). Two asterisks (**) indicate p value smaller than 0.01 ($p < 0.01$). Three asterisks (***) indicate p value smaller than 0.001 ($p < 0.001$). See also Figure S5.

that GATA3 may be a target of BMP signaling. In support of this conjecture, exogenous BMP4 induced expression of ID1, an established BMP target (Hollnagel et al., 1999; Ying et al., 2003), in cultured interstitial cells, and elevated GATA3 levels (Figures 5K, 5L, and S5E). To examine a possible BMP4 GATA3 link, LDN-193189 was added to inhibit BMP type 1 receptor/phospho-SMAD activity in the presence of BMP4 (Brown et al., 2015; Cuny et al., 2008; Yu et al., 2008). As expected, LDN-193189 inhibited expression of the BMP-target *ID1* (Figure S5E). In contrast, qPCR measurement indicated that *GATA3* expression was unaltered suggesting that BMP4 elevation of GATA3 is independent of pSMAD1/5 activity (Figure S5E). BMPs have also been reported to act through Smad-independent ERK, p38, JNK, and SAPK MAPK pathways (Brown et al., 2015; Oxburgh et al., 2011; Leung-Hagesteijn et al., 2005; Herpin and Cunningham, 2007; Otani et al., 2007). To address this possibility, the UO126 MEK inhibitor was added to block ERK activity in the presence of BMP4. As expected, UO126 did not perturb BMP4-induced ID1 levels, but GATA3 levels were reduced (Figure S5E). However, UO126 alone was sufficient to increase GATA3 to a similar level as BMP4 treatment suggesting that multiple context-dependent signaling inputs may be involved in GATA3 regulation. BMPs are known to induce GATA3 (Peng et al., 2015; Lichtner et al., 2013) and act synergistically with p38 and ERK in some contexts (Brown et al., 2015; Xu et al., 2008; Shim et al., 2009). There are likely other sources of BMP4 (Raatikainen-Ahokas et al., 2000) and other signals that regulate GATA3 in the mesangium (Moriguchi et al., 2016; Van Esch et al., 2000). *BMP7* is involved in kidney development and disease (Dudley et al., 1999; Fetting et al., 2014; Godin et al., 1998; Oxburgh et al., 2005) (Figures 4G, 4H, S5F, and S5G), is expressed in later podocyte development (GS7) (Figure 3B), and along with BMP4 can induce pERK1/2 and p38 in mouse mesangial cells (Otani et al., 2007) suggesting mesangial BMP responsiveness is likely conserved in mammals.

DISCUSSION

The kidney's filter is a key target for re-building kidney function. The findings here inform on cell interactions that may facilitate this goal (Van Den Berg et al., 2018; Morizane et al., 2017). The single-nuclear transcriptional profiling reported here complements approaches from our group and others (Adam et al., 2017; Combes et al., 2019; Karaiskos et al., 2018; Lindström et al., 2018a, 2018b, 2018c; Menon et al., 2018; O'brien et al., 2018; Rutledge et al., 2017; Wilson and Humphreys, 2019; Wu et al., 2018, 2019) to identify previously unappreciated factors mediating formation of the renal filter. FBLN2, NTN4, and BMP4 are expressed by developing podocytes concomitant with angioblast and interstitial cell recruitment expressing cognate interacting factors indicating related and potentially concerted actions in the establishment of the glomerular filter (Figure 1). The *in vitro* studies support their actions on endothelial or mesangial cell programs. Mutations for mouse Fibulins 1, 3, 4, and 5 have strong pleiotropic phenotypes including hemorrhages in multiple tissues and defects in the capillaries heart, lung, and kidney including impaired formation of glomerular capillaries and abnormal cell junctions in *Fbln1* mutants (Kostka et al., 2001). However, in mouse, *Fbln2* mutants are viable with no reported kidney phenotype and *Fbln2* is localized quite differently in the mouse kidney (Olijnyk et al., 2014) when compared with its human ortholog. We hypothesize that developmentally restricted expression of *FBLN2* may perform highly specialized functions directing glomerular vascularization in human kidney development replacing some of the functions of Fbln1 in mouse. Thus far, human *FBLN2* has not been linked to human disease or kidney function (de Vega et al., 2009) but could be uncovered by genome-wide association study (GWAS)-powered investigations. However, FBLN2 has been shown

to exhibit properties in non-kidney systems similar to those demonstrated here. FBLN2 regulates invasion, migration, and/or adhesion of astrocytes, keratinocytes, and cancer cells and is linked to wound healing cells (de Vega et al., 2009, Fontanil et al., 2017; Law et al., 2012; Olijnyk et al., 2014; Schaeffer et al., 2018). *FBLN2* also shows alternate splice isoform abundance in mouse versus human (Grässel et al., 1999; Pfaff et al., 1995). In contrast, disruption of *Bmp4* leads to mesangial and RC defects in the mouse (Ueda et al., 2008), suggesting that BMP4's function in human and mouse may be a conserved requirement for glomerulus development. A current goal for kidney translational research is to vascularize pluripotent-derived kidney tissues *in vitro* and replicate glomerular function but has thus far eluded our best efforts and impedes clinical application of kidney organoids. Thus, there is an acute need for knowledge of mechanisms sufficient to direct vascularization of kidney tissue types *in vitro*, and our work presented here has identified three potential candidates. Future studies will focus on regulation of FBLN2, NTN4, and BMP4 to induce *in vitro* assembly of glomerular capillary formation, maintenance, and function. In conclusion, these studies highlight the power of single-cell analysis in the understanding of human organogenesis, predicting cell interactions and distinct pathways of action not observed in the mouse model system.

Limitations of the Study

Deidentified primary human fetal kidney tissue for nuclei profiling, imaging, and *in vitro* culture were received on a case-by-case basis. Limitations on the availability of tissue samples and variability in sample age and sex precluded a detailed mechanistic follow-up of the preliminary findings of BMP4-mediated regulation of mesangial GATA3 expression. Additional studies will be essential to clarify the pathway(s) of action of the signaling activities identified here and how these factors may cooperate with a broader range of signals within the developing glomerular environment. Here, GATA3 upregulation within interstitial cells could facilitate unbiased systematic screening to broadly explore pathway actions in future work.

METHODS

All methods can be found in the accompanying Transparent Methods supplemental file.

DATA AND CODE AVAILABILITY

snDrop-seq raw sequencing files and associated annotated count matrix are available from the Gene Expression Omnibus: GSE114569 and NCBI: 19094300.

SUPPLEMENTAL INFORMATION

Supplemental Information can be found online at https://doi.org/10.1016/j.isci.2019.09.029.

ACKNOWLEDGMENTS

We thank all members of the McMahon and Zhang laboratories including Nils Lindstrom, Pietro Cippa, and Andrew Ransick for critical input. We thank Dr. Seth Ruffins for help with confocal imaging and deconvolution. We thank Mickey Huang for High-Content imaging. Work in A.P.M.'s laboratory was supported by grants from the National Institutes of Health (NIH) (DK107350, DK094526, DK110792). A.D.K. was supported by the NIH (5F32DK109616-02) and the University of Southern California (USC) Stem Cell postdoctoral fellowship from the Hearst Foundation.

AUTHOR CONTRIBUTIONS

A.D.K., B.B.L., K.Z, and A.P.M. planned experiments and analyzed data. B.B.L., A.D.K., and Y.W. assembled the figures. B.B.L., A.D.K., S.C., Y.W., R.K.P., J.G, T.T., and J.A.M. collected data. M.E.T. and B.G. provided embryonic and fetal kidneys. A.D.K., B.B.L., K.Z. and A.P.M. wrote the manuscript incorporating input from all authors.

DECLARATION OF INTERESTS

The authors declare no competing interests.

Received: July 9, 2019
Revised: August 21, 2019
Accepted: September 23, 2019
Published: October 25, 2019

REFERENCES

Adam, M., Potter, A.S., and Potter, S.S. (2017). Psychrophilic proteases dramatically reduce single-cell RNA-seq artifacts: a molecular atlas of kidney development. Development *144*, 3625–3632.

Barkefors, I., Le Jan, S., Jakobsson, L., Hejll, E., Carlson, G., Johansson, H., Jarvius, J., Park, J.W., Li Jeon, N., and Kreuger, J. (2008). Endothelial cell migration in stable gradients of vascular endothelial growth factor A and fibroblast growth factor 2: effects on chemotaxis and chemokinesis. J. Biol. Chem. *283*, 13905–13912.

Becht, E., Mcinnes, L., Healy, J., Dutertre, C.A., Kwok, I.W.H., Ng, L.G., Ginhoux, F., and Newell, E.W. (2018). Dimensionality reduction for visualizing single-cell data using UMAP. Nat. Biotechnol. *37*, 38–44.

Berry, R., Harewood, L., Pei, L., Fisher, M., Brownstein, D., Ross, A., Alaynick, W.A., Moss, J., Hastie, N.D., Hohenstein, P., et al. (2011). ESRRG functions in early branch generation of the ureteric bud and is essential for normal development of the renal papilla. Hum. Mol. Genet. *20*, 917–926.

Bjarnegård, M., Enge, M., Norlin, J., Gustafsdottir, S., Fredriksson, S., Abramsson, A., Takemoto, M., Gustafsson, E., Fässler, R., and Betsholtz, C. (2004). Endothelium-specific ablation of PDGFB leads to pericyte loss and glomerular, cardiac and placental abnormalities. Development *131*, 1847–1857.

Boualia, S.K., Gaitan, Y., Tremblay, M., Sharma, R., Cardin, J., Kania, A., and Bouchard, M. (2013). A core transcriptional network composed of Pax2/8, Gata3 and Lim1 regulates key players of pro/mesonephros morphogenesis. Dev. Biol. *382*, 555–566.

Brenner, B.M., Lawler, E.V., and Mackenzie, H.S. (1996). The hyperfiltration theory: a paradigm shift in nephrology. Kidney Int. *49*, 1774–1777.

Brown, J.C., Sasaki, T., Göhring, W., Yamada, Y., and Timpl, R. (1997). The C-terminal domain V of perlecan promotes beta1 integrin-mediated cell adhesion, binds heparin, nidogen and fibulin-2 and can be modified by glycosaminoglycans. Eur. J. Biochem. *250*, 39–46.

Brown, A.C., Muthukrishnan, S.D., and Oxburgh, L. (2015). A synthetic niche for nephron progenitor cells. Dev. Cell *34*, 229–241.

Chen, L., and Al-Awqati, Q. (2005). Segmental expression of Notch and Hairy genes in nephrogenesis. Am. J. Physiol. Renal. Physiol. *288*, F939–F952.

Chen, Z., Migeon, T., Verpont, M.C., Zaidan, M., Sado, Y., Kerjaschki, D., Ronco, P., and Plaisier, E. (2016). HANAC syndrome Col4a1 mutation causes neonate glomerular hyperpermeability and adult glomerulocystic kidney disease. J. Am. Soc. Nephrol. *27*, 1042–1054.

Chew, C., and Lennon, R. (2018). Basement membrane defects in genetic kidney diseases. Front. Pediatr. *6*, 11.

Combes, A.N., Zappia, L., Er, P.X., Oshlack, A., and Little, M.H. (2019). Single-cell analysis reveals congruence between kidney organoids and human fetal kidney. Genome Med. *11*, 3.

Cuny, G.D., Yu, P.B., Laha, J.K., Xing, X., Liu, J.F., Lai, C.S., Deng, D.Y., Sachidanandan, C., Bloch, K.D., and Peterson, R.T. (2008). Structure-activity relationship study of bone morphogenetic protein (BMP) signaling inhibitors. Bioorg. Med. Chem. Lett. *18*, 4388–4392.

Dahl, U., Sjödin, A., Larue, L., Radice, G.L., Cajander, S., Takeichi, M., Kemler, R., and Semb, H. (2002). Genetic dissection of cadherin function during nephrogenesis. Mol. Cell Biol. *22*, 1474–1487.

de Vega, S., Iwamoto, T., and Yamada, Y. (2009). Fibulins: multiple roles in matrix structures and tissue functions. Cell Mol Life Sci *66*, 1890–1902.

Douglass, S., Goyal, A., and Iozzo, R.V. (2015). The role of perlecan and endorepellin in the control of tumor angiogenesis and endothelial cell autophagy. Connect Tissue Res. *56*, 381–391.

Dudley, A.T., Godin, R.E., and Robertson, E.J. (1999). Interaction between FGF and BMP signaling pathways regulates development of metanephric mesenchyme. Genes Dev. *13*, 1601–1613.

Eremina, V., Sood, M., Haigh, J., Nagy, A., Lajoie, G., Ferrara, N., Gerber, H.P., Kikkawa, Y., Miner, J.H., and Quaggin, S.E. (2003). Glomerular-specific alterations of VEGF-A expression lead to distinct congenital and acquired renal diseases. J. Clin. Invest. *111*, 707–716.

Fetting, J.L., Guay, J.A., Karolak, M.J., Iozzo, R.V., Adams, D.C., Maridas, D.E., Brown, A.C., and Oxburgh, L. (2014). FOXD1 promotes nephron progenitor differentiation by repressing decorin in the embryonic kidney. Development *141*, 17–27.

Fontanil, T., Álvarez-Teijeiro, S., Villaronga, M., Mohamedi, Y., Solares, L., Moncada-Pazos, A., Vega, J.A., García-Suárez, O., Pérez-Basterrechea, M., García-Pedrero, J.M., et al. (2017). Cleavage of Fibulin-2 by the aggrecanases ADAMTS-4 and ADAMTS-5 contributes to the tumorigenic potential of breast cancer cells. Oncotarget *8*, 13716–13729.

Franceschini, N., North, K.E., Kopp, J.B., Mckenzie, L., and Winkler, C. (2006). NPHS2 gene, nephrotic syndrome and focal segmental glomerulosclerosis: a HuGE review. Genet. Med. *8*, 63–75.

Godin, R.E., Takaesu, N.T., Robertson, E.J., and Dudley, A.T. (1998). Regulation of BMP7 expression during kidney development. Development *125*, 3473–3482.

Grässel, S., Sicot, F.X., Gotta, S., and Chu, M.L. (1999). Mouse fibulin-2 gene. Complete exon-intron organization and promoter characterization. Eur. J. Biochem. *263*, 471–477.

Harewood, L., Liu, M., Keeling, J., Howatson, A., Whiteford, M., Branney, P., Evans, M., Fantes, J., and Fitzpatrick, D.R. (2010). Bilateral renal agenesis/hypoplasia/dysplasia (BRAHD): postmortem analysis of 45 cases with breakpoint mapping of two de novo translocations. PLoS One *5*, e12375.

Herpin, A., and Cunningham, C. (2007). Cross-talk between the bone morphogenetic protein pathway and other major signaling pathways results in tightly regulated cell-specific outcomes. FEBS J. *274*, 2977–2985.

Hoang, S., Liauw, J., Choi, M., Guzman, R.G., and Steinberg, G.K. (2009). Netrin-4 enhances angiogenesis and neurologic outcome after cerebral ischemia. J. Cereb. Blood Flow Metab. *29*, 385–397.

Hollnagel, A., Oehlmann, V., Heymer, J., Rüther, U., and Nordheim, A. (1999). Id genes are direct targets of bone morphogenetic protein induction in embryonic stem cells. J. Biol. Chem. *274*, 19838–19845.

Igarashi, P., and Somlo, S. (2002). Genetics and pathogenesis of polycystic kidney disease. J. Am. Soc. Nephrol. *13*, 2384–2398.

Karaiskos, N., Rahmatollahi, M., Boltengagen, A., Liu, H., Hoehne, M., Rinschen, M., Schermer, B., Benzing, T., Rajewsky, N., Kocks, C., et al. (2018). A single-cell transcriptome atlas of the mouse glomerulus. J. Am. Soc. Nephrol. *29*, 2060–2068.

Kobayashi, A., Kwan, K.M., Carroll, T.J., Mcmahon, A.P., Mendelsohn, C.L., and Behringer, R.R. (2005). Distinct and sequential tissue-specific activities of the LIM-class homeobox gene Lim1 for tubular morphogenesis during kidney development. Development *132*, 2809–2823.

Kobayashi, A., Mugford, J.W., Krautzberger, A.M., Naiman, N., Liao, J., and Mcmahon, A.P. (2014). Identification of a multipotent self-renewing stromal progenitor population during mammalian kidney organogenesis. Stem Cell Reports *3*, 650–662.

Komaki, F., Miyazaki, Y., Niimura, F., Matsusaka, T., Ichikawa, I., and Motojima, M. (2013). Foxc1 gene null mutation causes ectopic budding and kidney hypoplasia but not dysplasia. Cells Tissues Organs *198*, 22–27.

Kostka, G., Giltay, R., Bloch, W., Addicks, K., Timpl, R., Fässler, R., and Chu, M.L. (2001). Perinatal lethality and endothelial cell abnormalities in several vessel compartments of fibulin-1-deficient mice. Mol. Cell Biol. *21*, 7025–7034.

Kume, T., Deng, K., and Hogan, B.L. (2000). Murine forkhead/winged helix genes Foxc1 (Mf1) and Foxc2 (Mfh1) are required for the early organogenesis of the kidney and urinary tract. Development *127*, 1387–1395.

Labastie, M.C., Catala, M., Gregoire, J.M., and Peault, B. (1995). The GATA-3 gene is expressed during human kidney embryogenesis. Kidney Int. *47*, 1597–1603.

Lake, B.B., Ai, R., Kaeser, G.E., Salathia, N.S., Yung, Y.C., Liu, R., Wildberg, A., Gao, D., Fung, H.L., Chen, S., et al. (2016). Neuronal subtypes and diversity revealed by single-nucleus RNA sequencing of the human brain. Science *352*, 1586–1590.

Lake, B.B., Codeluppi, S., Yung, Y.C., Gao, D., Chun, J., Kharchenko, P.V., Linnarsson, S., and Zhang, K. (2017). A comparative strategy for

single-nucleus and single-cell transcriptomes confirms accuracy in predicted cell-type expression from nuclear RNA. Sci. Rep. *7*, 6031.

Lake, B.B., Chen, S., Sos, B.C., Fan, J., Kaeser, G.E., Yung, Y.C., Duong, T.E., Gao, D., Chun, J., Kharchenko, P.V., and Zhang, K. (2018). Integrative single-cell analysis of transcriptional and epigenetic states in the human adult brain. Nat. Biotechnol. *36*, 70–80.

Lambert, E., Coissieux, M.M., Laudet, V., and Mehlen, P. (2012). Netrin-4 acts as a pro-angiogenic factor during zebrafish development. J. Biol. Chem. *287*, 3987–3999.

Law, E.W., Cheung, A.K., Kashuba, V.I., Pavlova, T.V., Zabarovsky, E.R., Lung, H.L., Cheng, Y., Chua, D., Lai-Wan Kwong, D., Tsao, S.W., et al. (2012). Anti-angiogenic and tumor-suppressive roles of candidate tumor-suppressor gene, Fibulin-2, in nasopharyngeal carcinoma. Oncogene *31*, 728–738.

Leimeister, C., Schumacher, N., and Gessler, M. (2003). Expression of Notch pathway genes in the embryonic mouse metanephros suggests a role in proximal tubule development. Gene Expr. Patterns *3*, 595–598.

Lejmi, E., Bouras, I., Camelo, S., Roumieux, M., Minet, N., Leré-Déan, C., Merkulova-Rainon, T., Autret, G., Vayssettes, C., Clement, O., et al. (2014). Netrin-4 promotes mural cell adhesion and recruitment to endothelial cells. Vasc. Cell *6*, 1.

Leung-Hagesteijn, C., Hu, M.C., Mahendra, A.S., Hartwig, S., Klamut, H.J., Rosenblum, N.D., and Hannigan, G.E. (2005). Integrin-linked kinase mediates bone morphogenetic protein 7-dependent renal epithelial cell morphogenesis. Mol. Cell Biol. *25*, 3648–3657.

Levéen, P., Pekny, M., Gebre-Medhin, S., Swolin, B., Larsson, E., and Betsholtz, C. (1994). Mice deficient for PDGF B show renal, cardiovascular, and hematological abnormalities. Genes Dev. *8*, 1875–1887.

Lichtner, B., Knaus, P., Lehrach, H., and Adjaye, J. (2013). BMP10 as a potent inducer of trophoblast differentiation in human embryonic and induced pluripotent stem cells. Biomaterials *34*, 9789–9802.

Lindahl, P., Hellström, M., Kalén, M., Karlsson, L., Pekny, M., Pekna, M., Soriano, P., and Betsholtz, C. (1998). Paracrine PDGF-B/PDGF-Rbeta signaling controls mesangial cell development in kidney glomeruli. Development *125*, 3313–3322.

Lindström, N.O., De Sena Brandine, G., Tran, T., Ransick, A., Suh, G., Guo, J., Kim, A.D., Parvez, R.K., Ruffins, S.W., Rutledge, E.A., et al. (2018a). Progressive recruitment of mesenchymal progenitors reveals a time-dependent process of cell fate acquisition in mouse and human nephrogenesis. Dev. Cell *45*, 651–660.e4.

Lindström, N.O., Guo, J., Kim, A.D., Tran, T., Guo, Q., De Sena Brandine, G., Ransick, A., Parvez, R.K., Thornton, M.E., Basking, L., et al. (2018b). Conserved and divergent features of mesenchymal progenitor cell types within the cortical nephrogenic niche of the human and mouse kidney. J. Am. Soc. Nephrol. *29*, 806–824.

Lindström, N.O., Mcmahon, J.A., Guo, J., Tran, T., Guo, Q., Rutledge, E., Parvez, R.K., Saribekyan, G., Schuler, R.E., Liao, C., et al. (2018c). Conserved and divergent features of human and mouse kidney organogenesis. J. Am. Soc. Nephrol. *29*, 785–805.

Lindström, N.O., Tran, T., Guo, J., Rutledge, E., Parvez, R.K., Thornton, M.E., Grubbs, B., Mcmahon, J.A., and Mcmahon, A.P. (2018d). Conserved and divergent molecular and anatomic features of human and mouse nephron patterning. J. Am. Soc. Nephrol. *29*, 825–840.

Liu, Z., Chen, S., Boyle, S., Zhu, Y., Zhang, A., Piwnica-Worms, D.R., Ilagan, M.X., and Kopan, R. (2013). The extracellular domain of Notch2 increases its cell-surface abundance and ligand responsiveness during kidney development. Dev. Cell *25*, 585–598.

Lo, H.M., Hwang, T.L., and Wu, W.B. (2017). A phenanthrene derivative, 5,7-dimethoxy-1,4-phenanthrenequinone, inhibits cell adhesion molecule expression and migration in vascular endothelial and smooth muscle cells. Pharmacology *99*, 291–302.

Lu, X., Le Noble, F., Yuan, L., Jiang, Q., De Lafarge, B., Sugiyama, D., Bréant, C., Claes, F., De Smet, F., Thomas, J.L., et al. (2004). The netrin receptor UNC5B mediates guidance events controlling morphogenesis of the vascular system. Nature *432*, 179–186.

Menon, R., Otto, E.A., Kokoruda, A., Zhou, J., Zhang, Z., Yoon, E., Chen, Y.C., Troyanskaya, O., Spence, J.R., Kretzler, M., and Cebrián, C. (2018). Single-cell analysis of progenitor cell dynamics and lineage specification in the human fetal kidney. Development *145*, 1–14.

Michos, O., Gonçalves, A., Lopez-Rios, J., Tiecke, E., Naillat, F., Beier, K., Galli, A., Vainio, S., and Zeller, R. (2007). Reduction of BMP4 activity by gremlin 1 enables ureteric bud outgrowth and GDNF/WNT11 feedback signalling during kidney branching morphogenesis. Development *134*, 2397–2405.

Miyazaki, Y., Oshima, K., Fogo, A., Hogan, B.L., and Ichikawa, I. (2000). Bone morphogenetic protein 4 regulates the budding site and elongation of the mouse ureter. J. Clin. Invest. *105*, 863–873.

Mongiat, M., Sweeney, S.M., San Antonio, J.D., Fu, J., and Iozzo, R.V. (2003). Endorepellin, a novel inhibitor of angiogenesis derived from the C terminus of perlecan. J. Biol. Chem. *278*, 4238–4249.

Moriguchi, T., Yu, L., Otsuki, A., Ainoya, K., Lim, K.C., Yamamoto, M., and Engel, J.D. (2016). Gata3 hypomorphic mutant mice rescued with a yeast artificial chromosome transgene suffer a glomerular mesangial cell defect. Mol. Cell Biol. *36*, 2272–2281.

Morizane, R., Lam, A.Q., Freedman, B.S., Kishi, S., Valerius, M.T., and Bonventre, J.V. (2015). Nephron organoids derived from human pluripotent stem cells model kidney development and injury. Nat. Biotechnol. *33*, 1193–1200.

Morizane, R., Miyoshi, T., and Bonventre, J.V. (2017). Concise review: kidney generation with human pluripotent stem cells. Stem Cells *35*, 2209–2217.

Motojima, M., Kume, T., and Matsusaka, T. (2017). Foxc1 and Foxc2 are necessary to maintain glomerular podocytes. Exp. Cell Res. *352*, 265–272.

Mundel, P., Heid, H.W., Mundel, T.M., Krüger, M., Reiser, J., and Kriz, W. (1997). Synaptopodin: an actin-associated protein in telencephalic dendrites and renal podocytes. J. Cell Biol. *139*, 193–204.

Nacht, M., St Martin, T.B., Byrne, A., Klinger, K.W., Teicher, B.A., Madden, S.L., and Jiang, Y. (2009). Netrin-4 regulates angiogenic responses and tumor cell growth. Exp. Cell Res. *315*, 784–794.

Narlis, M., Grote, D., Gaitan, Y., Boualia, S.K., and Bouchard, M. (2007). Pax2 and pax8 regulate branching morphogenesis and nephron differentiation in the developing kidney. J. Am. Soc. Nephrol. *18*, 1121–1129.

O'brien, L.L., Guo, Q., Bahrami-Samani, E., Park, J.S., Hasso, S.M., Lee, Y.J., Fang, A., Kim, A.D., Guo, J., Hong, T.M., et al. (2018). Transcriptional regulatory control of mammalian nephron progenitors revealed by multi-factor cistromic analysis and genetic studies. PLoS Genet. *14*, e1007181.

Olijnyk, D., Ibrahim, A.M., Ferrier, R.K., Tsuda, T., Chu, M.L., Gusterson, B.A., Stein, T., and Morris, J.S. (2014). Fibulin-2 is involved in early extracellular matrix development of the outgrowing mouse mammary epithelium. Cell. Mol. Life Sci. *71*, 3811–3828.

Otani, H., Otsuka, F., Inagaki, K., Takeda, M., Miyoshi, T., Suzuki, J., Mukai, T., Ogura, T., and Makino, H. (2007). Antagonistic effects of bone morphogenetic protein-4 and -7 on renal mesangial cell proliferation induced by aldosterone through MAPK activation. Am. J. Physiol. Renal. Physiol. *292*, F1513–F1525.

Oxburgh, L., Dudley, A.T., Godin, R.E., Koonce, C.H., Islam, A., Anderson, D.C., Bikoff, E.K., and Robertson, E.J. (2005). BMP4 substitutes for loss of BMP7 during kidney development. Dev. Biol. *286*, 637–646.

Oxburgh, L., Brown, A.C., Fetting, J., and Hill, B. (2011). BMP signaling in the nephron progenitor niche. Pediatr. Nephrol. *26*, 1491–1497.

Padgett, R.W., Wozney, J.M., and Gelbart, W.M. (1993). Human BMP sequences can confer normal dorsal-ventral patterning in the Drosophila embryo. Proc. Natl. Acad. Sci. U S A *90*, 2905–2909.

Pan, T.C., Sasaki, T., Zhang, R.Z., Fässler, R., Timpl, R., and Chu, M.L. (1993). Structure and expression of fibulin-2, a novel extracellular matrix protein with multiple EGF-like repeats and consensus motifs for calcium binding. J. Cell Biol. *123*, 1269–1277.

Park, J.S., Valerius, M.T., and Mcmahon, A.P. (2007). Wnt/beta-catenin signaling regulates nephron induction during mouse kidney development. Development *134*, 2533–2539.

Park, J., Shrestha, R., Qiu, C., Kondo, A., Huang, S., Werth, M., Li, M., Barasch, J., and Suszták, K. (2018). Single-cell transcriptomics of the mouse

kidney reveals potential cellular targets of kidney disease. Science *360*, 758–763.

Peng, T., Zhu, G., Dong, Y., Zeng, J., Li, W., Guo, W., Chen, Y., Duan, M., Hocher, B., and Xie, D. (2015). BMP4: a possible key factor in differentiation of auditory neuron-like cells from bone-derived mesenchymal stromal cells. Clin. Lab. *61*, 1171–1178.

Pfaff, M., Sasaki, T., Tangemann, K., Chu, M.L., and Timpl, R. (1995). Integrin-binding and cell-adhesion studies of fibulins reveal a particular affinity for alpha IIb beta 3. Exp. Cell Res. *219*, 87–92.

Piscione, T.D., Wu, M.Y., and Quaggin, S.E. (2004). Expression of hairy/enhancer of split genes, Hes1 and Hes5, during murine nephron morphogenesis. Gene Expr. Patterns *4*, 707–711.

Plachov, D., Chowdhury, K., Walther, C., Simon, D., Guenet, J.L., and Gruss, P. (1990). Pax8, a murine paired box gene expressed in the developing excretory system and thyroid gland. Development *110*, 643–651.

Poluzzi, C., Iozzo, R.V., and Schaefer, L. (2016). Endostatin and endorepellin: a common route of action for similar angiostatic cancer avengers. Adv. Drug Deliv. Rev. *97*, 156–173.

Qiu, X., Mao, Q., Tang, Y., Wang, L., Chawla, R., Pliner, H.A., and Trapnell, C. (2017). Reversed graph embedding resolves complex single-cell trajectories. Nat. Methods *14*, 979–982.

Raatikainen-Ahokas, A., Hytönen, M., Tenhunen, A., Sainio, K., and Sariola, H. (2000). BMP-4 affects the differentiation of metanephric mesenchyme and reveals an early anterior-posterior axis of the embryonic kidney. Dev. Dyn. *217*, 146–158.

Ranganathan, P., Mohamed, R., Jayakumar, C., Brands, M.W., and Ramesh, G. (2015). Deletion of UNC5B in kidney epithelium exacerbates diabetic nephropathy in mice. Am. J. Nephrol. *41*, 220–230.

Roselli, S., Heidet, L., Sich, M., Henger, A., Kretzler, M., Gubler, M.C., and Antignac, C. (2004). Early glomerular filtration defect and severe renal disease in podocin-deficient mice. Mol. Cell Biol. *24*, 550–560.

Rosenberg, P., Esni, F., Sjödin, A., Larue, L., Carlsson, L., Gullberg, D., Takeichi, M., Kemler, R., and Semb, H. (1997). A potential role of R-cadherin in striated muscle formation. Dev. Biol. *187*, 55–70.

Rutledge, E.A., Benazet, J.D., and Mcmahon, A.P. (2017). Cellular heterogeneity in the ureteric progenitor niche and distinct profiles of branching morphogenesis in organ development. Development *144*, 3177–3188.

Schaeffer, J., Tannahill, D., Cioni, J.M., Rowlands, D., and Keynes, R. (2018). Identification of the extracellular matrix protein Fibulin-2 as a regulator of spinal nerve organization. Dev. Biol. *442*, 101–114.

Schwab, K., Hartman, H.A., Liang, H.C., Aronow, B.J., Patterson, L.T., and Potter, S.S. (2006). Comprehensive microarray analysis of Hoxa11/Hoxd11 mutant kidney development. Dev. Biol. *293*, 540–554.

Sharif, B., and Barua, M. (2018). Advances in molecular diagnosis and therapeutics in nephrotic syndrome and focal and segmental glomerulosclerosis. Curr. Opin. Nephrol. Hypertens. *27*, 194–200.

Shim, J.H., Greenblatt, M.B., Xie, M., Schneider, M.D., Zou, W., Zhai, B., Gygi, S., and Glimcher, L.H. (2009). TAK1 is an essential regulator of BMP signalling in cartilage. EMBO J. *28*, 2028–2041.

Sison, K., Eremina, V., Baelde, H., Min, W., Hirashima, M., Fantus, I.G., and Quaggin, S.E. (2010). Glomerular structure and function require paracrine, not autocrine, VEGF-VEGFR-2 signaling. J. Am. Soc. Nephrol. *21*, 1691–1701.

Soriano, P. (1994). Abnormal kidney development and hematological disorders in PDGF beta-receptor mutant mice. Genes Dev. *8*, 1888–1896.

Taguchi, A., and Nishinakamura, R. (2015). Nephron reconstitution from pluripotent stem cells. Kidney Int. *87*, 894–900.

Takasato, M., Er, P.X., Chiu, H.S., Maier, B., Baillie, G.J., Ferguson, C., Parton, R.G., Wolvetang, E.J., Roost, M.S., Lopes, S.M., and Little, M.H. (2016). Kidney organoids from human iPS cells contain multiple lineages and model human nephrogenesis. Nature *536*, 238.

Ueda, H., Miyazaki, Y., Matsusaka, T., Utsunomiya, Y., Kawamura, T., Hosoya, T., and Ichikawa, I. (2008). Bmp in podocytes is essential for normal glomerular capillary formation. J. Am. Soc. Nephrol. *19*, 685–694.

Van Den Berg, C.W., Ritsma, L., Avramut, M.C., Wiersma, L.E., Van Den Berg, B.M., Leuning, D.G., Lievers, E., Koning, M., Vanslambrouck, J.M., Koster, A.J., et al. (2018). Renal subcapsular transplantation of PSC-derived kidney organoids induces neo-vasculogenesis and significant glomerular and tubular maturation in vivo. Stem Cell Reports *10*, 751–765.

Van Esch, H., Groenen, P., Nesbit, M.A., Schuffenhauer, S., Lichtner, P., Vanderlinden, G., Harding, B., Beetz, R., Bilous, R.W., Holdaway, I., et al. (2000). GATA3 haplo-insufficiency causes human HDR syndrome. Nature *406*, 419–422.

Wang, W., Reeves, W.B., and Ramesh, G. (2008). Netrin-1 and kidney injury. I. Netrin-1 protects against ischemia-reperfusion injury of the kidney. Am. J. Physiol. Renal. Physiol. *294*, F739–F747.

Wilson, P.D. (2004). Polycystic kidney disease: new understanding in the pathogenesis. Int. J. Biochem. Cell Biol. *36*, 1868–1873.

Wilson, P.C., and Humphreys, B.D. (2019). Kidney and organoid single-cell transcriptomics: the end of the beginning. Pediatr. Nephrol. 1–7.

Wu, H., Malone, A.F., Donnelly, E.L., Kirita, Y., Uchimura, K., Ramakrishnan, S.M., Gaut, J.P., and Humphreys, B.D. (2018a). Single-cell transcriptomics of a human kidney allograft biopsy specimen defines a diverse inflammatory response. J. Am. Soc. Nephrol. *29*, 2069–2080.

Wu, Y., Tamayo, P., and Zhang, K. (2018b). Visualizing and interpreting single-cell gene expression datasets with similarity weighted nonnegative embedding. Cell Syst. *7*, 656–666.e4.

Wu, H., Kirita, Y., Donnelly, E.L., and Humphreys, B.D. (2019). Advantages of single-nucleus over single-cell RNA sequencing of adult kidney: rare cell types and novel cell states revealed in fibrosis. J. Am. Soc. Nephrol. *30*, 23–32.

Xu, X., Han, J., Ito, Y., Bringas, P., Deng, C., and Chai, Y. (2008). Ectodermal Smad4 and p38 MAPK are functionally redundant in mediating TGF-beta/BMP signaling during tooth and palate development. Dev. Cell *15*, 322–329.

Yanagida-Asanuma, E., Asanuma, K., Kim, K., Donnelly, M., Young Choi, H., Hyung Chang, J., Suetsugu, S., Tomino, Y., Takenawa, T., Faul, C., and Mundel, P. (2007). Synaptopodin protects against proteinuria by disrupting Cdc42:IRSp53:Mena signaling complexes in kidney podocytes. Am. J. Pathol. *171*, 415–427.

Yarrow, J.C., Perlman, Z.E., Westwood, N.J., and Mitchison, T.J. (2004). A high-throughput cell migration assay using scratch wound healing, a comparison of image-based readout methods. BMC Biotechnol. *4*, 21.

Yin, Y., Sanes, J.R., and Miner, J.H. (2000). Identification and expression of mouse netrin-4. Mech. Dev. *96*, 115–119.

Ying, Q.L., Nichols, J., Chambers, I., and Smith, A. (2003). BMP induction of Id proteins suppresses differentiation and sustains embryonic stem cell self-renewal in collaboration with STAT3. Cell *115*, 281–292.

Yu, P.B., Deng, D.Y., Lai, C.S., Hong, C.C., Cuny, G.D., Bouxsein, M.L., Hong, D.W., Mcmanus, P.M., Katagiri, T., Sachidanandan, C., et al. (2008). BMP type I receptor inhibition reduces heterotopic [corrected] ossification. Nat. Med. *14*, 1363–1369.

Zhang, R.Z., Pan, T.C., Zhang, Z.Y., Mattei, M.G., Timpl, R., and Chu, M.L. (1994). Fibulin-2 (FBLN2): human cDNA sequence, mRNA expression, and mapping of the gene on human and mouse chromosomes. Genomics *22*, 425–430.

Zhong, J., Yang, H.C., and Fogo, A.B. (2017). A perspective on chronic kidney disease progression. Am. J. Physiol. Renal. Physiol. *312*, F375–F384.

ISCI, Volume *20*

Supplemental Information

Cellular Recruitment by Podocyte-Derived Pro-migratory Factors in Assembly of the Human Renal Filter

Albert D. Kim, Blue B. Lake, Song Chen, Yan Wu, Jinjin Guo, Riana K. Parvez, Tracy Tran, Matthew E. Thornton, Brendan Grubbs, Jill A. McMahon, Kun Zhang, and Andrew P. McMahon

Transparent Methods

Human Kidney Material

Consented, anonymized, human fetal tissue was obtained from elective terminations through collaborators at the Children's Hospital of Los Angeles following institutional review board assessment of the study. Gestational age was determined per guidelines specified by the American College of Obstetricians and Gynecologists using ultrasound, heel-to-toe, and crown-to-rump measurements following published CSs. Stages indicate the age of the embryo or fetus from the point of conception/fertilization. Samples from the Children's Hospital of Los Angeles were received immediately after elective terminations and transported on ice at 4°C in 10% FBS, 25 mM Hepes, high-glucose DMEM (SIGMA).

Sample isolation and nuclei preparation

Human cortical nephrogenic zone cells were isolated from 13-18 week fetal human kidneys using 10 mg/ml pancreatin (Sigma, P1625) and 2.5 mg/ml collagenase A (Roche, 11 088 793 001) enzyme mixture and filtered through 40 µm filter (BD Falcon 352340) as described previously (Brown et al., 2015). RCs were sieved from fetal kidneys by macerating on top of 100 µm filter (Falcon, 352360) with rubber plunger then flowing 5 ml of ice-cold Calcium/Magnesium free PBS through macerated tissue. The flow-through was then passed through a 70 µm filter (Falcon, 352350) to sieve RCs. The 70 µm filter was inverted over a 50 ml conical tube and 5 ml of ice-cold PBS was poured over the filter to retrieve RCs. RCs were spun down at 500 g for 10 minutes in swinging bucket rotor centrifuge. Nephrogenic cortex cells and RCs were cryopreserved with 10% FBS in DMEM or RNAlater and stored at -20 °C before subsequent nuclei extraction. Nuclei were isolated using nuclear extraction buffer (NEB) and used for snDrop-seq as described previously (Lake et al., 2016, Lake et al., 2017), with step-by-step protocols also available from https://kpmp.org/resources/.

snDrop-seq data processing and analyses

Paired-end sequencing reads were processed and mapped to the human genome (GENCODE GRCH38) as described previously (Lake et al., 2017) (software available at https://github.com/chensong611/Dropseq_pipeline) to generate a digital expression matrix of unique molecular identifier (UMI) counts for all detected genes and for all cell barcodes. Each cell barcode was then tagged by an associated library batch ID (Supplementary Table 1) and count matrices combined across independent experiments. Mitochondrial genes not expressed in nuclei and nuclei with fewer than 400 or greater than 5000 genes detected were omitted. Counts were then normalized to the total number of counts for each nucleus. For clustering, Pagoda2 (https://github.com/hms-dbmi/pagoda2) was used as described previously (Lake et al., 2017), with the exception that clusters having less than 50 data sets were excluded to remove outliers and possible multiplets. Two clusters (each consisting of 52 data sets each) that showed high ribosomal RNA content were also excluded. Further analyses were performed using Seurat software (V2.1.0) in R (https://github.com/satijalab/seurat) where counts for all cell barcodes used in Pagoda2 clustering were scaled by total UMI counts, multiplied by 10,000 and transformed to log space. Technical effects of batch and UMI coverage were regressed from scaled data using the RegressOut function and variable genes identified from a mean variability plot (Seurat). Cluster identities, top 150 principle components and t-SNE coordinates were imported into Seurat from Pagoda2 and differentially expressed genes (DEGs, adjusted p value < 0.05) between clusters (Supplementary Table 4) were calculated using a Wilcoxon rank sum test (Seurat) on genes detected in at least 25% of cells within a cluster. UMAP dimensional reduction was performed in Seurat (version 2.3.4) using the top 150 PCs identified using Pagoda2. Gene ontology analysis on all significant DEGs for each cluster was performed using https://toppgene.cchmc.org/ (Supplementary Table S5). Violin plots, dot plots, expression heatmap of top DEGs and feature plots were generated using Seurat. A pair-wise correlation plot for annotated clusters was performed using log-transformed cluster-averaged expression values for all DEGs having an adjusted p value less than 0.05 (Supplementary Table 4). SWNE was performed as described (https://yanwu2014.github.io/swne/) (Wu et al., 2018) and involved nonnegative matrix factorization (NMF)

to decompose the gene expression matrix into biologically relevant nonnegative factors. SWNE was then used to embed both the cells and the factors in a two-dimensional visualization, using a shared nearest neighbors (SNN) graph to ensure that cells that are close in the gene expression space are also close in the visualization. The nonnegative factors were annotated using the gene-factor loadings (analogous to using principal component loadings to interpret PCA) and projected as data points onto the visualization.

Developmental Trajectory Analyses

snDrop-seq UMI count matrices for select clusters were analyzed using Monocle software (Trapnell et al., 2014) (v2.4.0) in R according to the provided documentation (http://cole-trapnell-lab.github.io/monocle-release/) and with UMI counts modeled as a negative binomial distribution. For all nephrogenic lineages: ordering genes were determined as the top 800 differentially expressed genes (expressed in at least 10 nuclei) that were identified using the differentialGeneTest function (Monocle) between associated clusters (Pagoda2 defined) and that were ordered by their q values. Reduction to two dimensions was performed using the discriminative dimensionality reduction with trees (DDRTree) method. To identify genes varying between proximal and medial/distal branches of the trajectory, BEAM analysis (Monocle) was performed and genes showing significant q values (<0.01) were plotted using the plot_genes_branched_heatmap function. Differentially expressed genes between data sets occupying each branch (and compared against all remaining data sets) were further identified using the Wilcoxon rank sum test (Seurat). Genes showing significant variation by pseudotime (q value < 0.01) were identified, plotted using the plot pseudotime_heatmap function (Monocle) and genes showing intermediate expression profiles were selected manually. Trajectory analyses were subsequently repeated for the proximal branch (visceral and PE, ordering on the top 500 cluster-specific DEGs) and the medial/distal branch (proximal/medial/distal tubules, ordering on the top 1200 cluster-specific DEGs) as described above. To better understand gene expression dynamics specific to the podocyte lineage, the progenitor branch (from Plot 1, Supplementary Fig. 3a) and the podocyte and progenitor branches (from Plot 2, Supplementary Fig. 3a) were selected for combined reanalysis. For this, cNPCs were excluded, the remaining cluster identities were merged into broad categories (NPC, dNPC, DT, MDT, PE, POD, PT), and the top 500 differentially expressed genes between the merged clusters (q values less than 0.01) were used for ordering as described above. To select for gene sets differentially expressed along this trajectory, genes showing differential expression according to pseudotime (using the differentialGeneTest function in Monocle) having q values less than 0.1 were segregated into 8 groups using hierarchical clustering (plot_pseudotime_heatmap function in Monocle). Trajectory analysis was also performed on the interstitial clusters (excluding cycling interstitial cells to prevent ordering based on cellular division) using the top 1000 cluster-specific DEGs. For differential expression between branch occupied data sets using the Wilcoxon rank sum test (Seurat), the initial branch representing a potential stressed INT-3 population was excluded. Differentially expressed genes for all trajectory analyses are provided as Supplementary Tables and are indicated in Supplementary Fig. 3. All gene ontology analyses were performed using https://toppgene.cchmc.org/.

Statistics

snDrop-seq analyses were performed on 7018 data sets combined across 4 different individuals: (1) a 16.5 week renal cortex sample processed over a single experiment and over 8 libraries; (2) a 14.4 week renal cortex sample processed over 2 independent experiments and 6 libraries; (3) a 13 week dissected glomerular and biopsy punch sample processed over a single experiment and 2 libraries; (4) a 15 week dissected glomerular sample processed over a single experiment and a single library. See Supplementary Table S1.

Data Availability

snDrop-seq raw sequencing files and associated annotated count matrix are available from the Gene Expression Omnibus under the accession code GSE114569 and NCBI tracking system #19094300.

Sample preparation for sectioning and immunofluorescence

For *in situ* and immunoanalysis, human and mouse kidney samples were fixed in 4% formaldehyde overnight at 4°C with mixed-motion provide by a Nutator (Thomas Scientific). Samples were subsequently washed twice with PBS then placed in 30% sucrose, 24 hours for week 8 and 48 hours for week 16 samples, prior to embedding and freezing in Optimal Cutting Temperature compound (Tissue-Tek, 4583). All samples were sectioned at 10 µm intervals, placed on slides, and stored at -80°C before use. Immunofluorescent detection of target antigens was largely performed as previously described with some modifications. Slides were washed in PBS for 5 min to remove OCT and subsequently blocked for 30 min in PBS with 2% SEA block (ThermoFisher Scientific, 37527) and 0.25% TritonX100. Primary antibodies were diluted in the blocking solution and applied to the samples overnight at 4 °C: WT1 (Abcam, AF647, ab89901, 1:1000), VEGFA (GeneTex, AF488, GTX54662, 1:200), PDGF-B (Novus Biologicals, AF594, MM0014-5F66, 1:200), SIX2 (MyBiosource, AF488, MBS610128, 1:1000), JAG1 (R&D, AF633, 1:300), LTBP1 (MyBioSource, AF555, MBS9129121, 1:200), PECAM1 (BD, AF555, 555444, 1:200), LRP2 (MyBiosource, AF488, MBS690201, 1:1000), CDH4 (MyBiosource, AF555, MBS855956, 1:300), ESRRG (Abcam, AF555, ab491291, 1:1000), PKHD1 (Thermofisher, AF555, PA5-56682, 1:1000), GATA3 (R&D, AF633, AF2605, 1:300), COL4A1 (Abcam, AF555, ab189408, 1:400), MAFB (Santa Cruz, AF633, sc-10022, 1:300), PAMR1 (Proteintech, AF555, 55310-1-AP, 1:800), CDH6 (R&D, AF633, AF2715, 1:300), PDGFRB (R&D, AF488, AF385, 1:300), HSPG2/Perlecan (R&D, AF555, AF2364-SP, 1:100), NTN4 (R&D, AF633, AF1254, 1:100), UNC5B (Bioss antibodies, AF555, bs-11492R, 1:200), REN (R&D, AF409, 1:300), and VEGFR2 (Cell Signaling, 24791, 1:300). Mouse samples were stained with Fbln2 (Santa Cruz, AF555, sc-271843, 1:200), Mafb (same as human, AF633), and Jag1 (Cell Signaling, AF488, 70109, 1:200). After incubation in primary antibodies the samples were washed 3 times in PBS with 0.25% TritonX100 (PBT). Secondary antibodies were diluted in the blocking solution and applied to the sample for 1 hour at room temperature. All secondary antibodies were purchased from Molecular Probes ThermoFisher Scientific and used at a 1:1000 dilution. Nuclei were stained with 1 µg/ml Hoechst 33342 (Invitrogen) in PBS for 5 min before a final PBS wash. Deconvolution of confocal images (in Fig. S2) was performed with Huygens Deconvolution (https://svi.nl/HuygensDeconvolution) using default settings.

Immunohistochemical staining

Immunohistochemical staining was performed with 2% SEA block (ThermoFisher Scientific, 37527) in 0.1% TBST and blocking of endogenous peroxidase activity with 3% H2O2 for 10 minutes. Phospho-Smad1/5 antibody (Cell Signaling, 9516S) or phospho-MAPK (Cell Signaling, 4370) was developed with standard protocol for Avidin-Biotin Complex ABC Kit (Vector #PK6100), and biotinylated rabbit antibody (Jackson Immuno Research Labs # 711-065-152) with DAB (Abcam #ab64238). PDGFRB (R&D, AF385) was developed with anti-goat Alkaline Phosphatase (Novus, NBP1-74812) with NTMT (Sigma, B5655-25TAB) and imaged on Zeiss Axioscan.

Conventional and RNAscope *in situ* hybridization

Conventional *in situ* were performed on frozen sectioned samples as previously described (https://www.gudmap.org/Research/Protocols/McMahon.html). For RNAscope *in situ* hybridization probes for PAMR1 (ACDBio, 454301), COL4A1 (ACDBio, 461881) were used while LTBP1, CDH4, ESRRG, PKHD1 were custom designed by ACDBio for this study. 2.5 Duplex Assay was performed and counterstained with Nuclear Fast Red (Vector, H3403) and imaged on Zeiss Axio Scan.Z1 Slide Scanner.

Image preparation for publishing declaration

2D sectional images were opened and processed in Leica LAS X, Zeiss ZEN, Adobe Photoshop, Adobe Illustrator, Huygens Deconvolution, and ImageJ.

Human fetal kidney endothelial and interstitial cell isolation and culture

Endothelial and interstitial cells were magnetically purified from cortical nephrogenic zone cells from two independent human fetal kidney samples via autoMACS Pro Separator and anti-CD144 (VECAD) PE-conjugated antibodies (Miltenyi Biotec, 130-100-716) and CD140b (PDGFRB) PE-conjugated antibodies (Miltenyi Biotec, 130-105-321) using positive selection. Primary HFK endothelial cells were cultured with Endothelial Cell Growth Medium (ECGM) with provided growth supplement (Promocell, C-22010), interstitial cells were cultured with MEM α, GlutaMAX™ Supplement, no nucleosides (Thermofisher, 32561037) supplemented with 10% Fetal Bovine Serum. Endothelial or interstitial cells were plated on 0.1% gelatin, cultured at 37 °C 5% CO_2 in 75 cm^2 tissue culture flasks and passaged up to four times prior to in vitro experiments. All assays were performed in triplicate.

Matrigel Migration assay

Assay was performed in triplicate as described (Finkenzeller et al., 2012) with the following modifications. Growth factor reduced Matrigel (Corning, 354277) was thawed overnight at 4 C and diluted at 1:20 in ECGM without growth supplement and 100 ul was spread over a 24-well size Transwell chamber with 8 µm pore size (Falcon, 353097) and allowed to equilibrate overnight. The chamber was inserted into a 24 well culture dish containing ECGM without growth supplement and supplemented with 50 ng/ml VEGFA (R&D, 293-VE-010), 100 ng/ml VEGFA blocking antibody (R&D, MAB293-SP), 30 ng/ml FGF2 (Peprotech, 100-18B), 30 ng/ml PDGF-bb (Peprotech, 100-14B), 22.5 and 75 ng/ml FBLN2 (Mybiosource, MBS2011606), 15 and 150 ng/ml NTN4 (R&D, 1254-N4-025), 5 and 50 ng/ml BMP4 (R&D, 314-BP-010). $2.5x10^5$ endothelial and/or interstitial cells were incubated in Transwell chamber for 6 hours at 37 °C in 5% CO_2. Unmigrated cells were removed from upper chamber, migrated cells were fixed with 4% PFA for 10 minutes then stained with DAPI and the entire Transwell was imaged with 4x objective on ImagXpress (https://www.nikoninstruments.com/). Total migrated cell numbers were quantified in ImageJ using the Analyze Particles function (http://rsb.info.nih.gov).

Matrigel endothelial tube formation assay

Assay was performed as described (Finkenzeller et al., 2012) with the following modifications. Matrigel was spread evenly over each well of a 96-well plate and allowed to solidify for 30 minutes at 37 °C. $1x10^5$ primary endothelial cells were seeded in triplicate into each well with ECGM without supplement and with factors indicated. Plates were incubated for 24 hours at 37 °C in 5% CO_2 then imaged by ImagXpress High-Content Analysis system with 20x objective and analyzed using ImageJ. For quantification the entire field was imaged and total length of endothelial tubes and number of branch points was manually quantified (n=3). Results were expressed as means ± standard deviation with significance calculated for differences between control and experimental groups.

BrdU inclusion assay

$1x10^5$ primary endothelial or interstitial cells were plated in triplicate into 0.1% gelatin-coated 96 well plates with basal media supplemented with 2% Fetal Bovine Serum and factors indicated. Cells were cultured for 24 hours at 37 °C in 5% CO_2 then stained for Brdu according to manufacturers' instructions for 2 hours (Thermofisher, B23151). Cells were fixed, stained with anti-BrdU (BD, 555627, 1:1000), anti-PECAM1, and/or anti-PDGFRB, and DAPI and imaged with 10x objective on ImagXpress. Fields from each plate were analyzed using Imaris software to quantitate percent of nuclei that were BrdU positive.

Lamellar extension assay

Experiments were performed similarly to a previous study (Yarrow et al., 2004) with the following modifications. Primary endothelial and/or interstitial cells were plated in triplicate into 0.1% gelatin-coated 96 well plates and allowed to grow to confluency with growth media. Prior to wound healing cells were starved of ECGM growth supplement or serum for 24 hours. Confluent cells were then scratched with a P1000 pipette tip and replaced with serum free media supplemented with indicated factors and/or inhibitors including DMPQ dihydrochloride (Sigma, SML0334-5MG), LDN-193189 (Stemgent, 04-0074-02), U0126 (Sigma, 19-147), and/or Endorepellin (R&D, 2364-ER-050). Cells were allowed to migrate for 0 or 7 hours then fixed and stained with Phalloidin 647 (Thermofisher, A22287, 1:1000) and DAPI and imaged with 10x objective on Leica SP8. Quantitation of wound healing was performed by measuring Actin- and DAPI- area in wounds in ImageJ, calculating the area differential, then dividing by the length of the wound to calculate average lamellar cell extension length.

Cell Adhesion assay

Individual wells of Immulon 4 HBX 96 well plates (Thermofisher, 3855) were coated with 10 ug/ml BMP4, NTN4, FBLN2, or BSA in 10 mM Acetic Acid at 4 C overnight. Protein was aspirated then nonspecific binding of cells to plate were blocked with 5% BSA for 1 hour. Wells were washed three times with PBS. $3x10^5$ primary endothelial or interstitial cells were plated in triplicate onto coated plates in serum free MEM α. Cells allowed to attach at room temperature for 1 hour then non-adherent cells were washed off three times with PBS and counted manually. Cells were fixed, stained with anti-FBLN2 and anti-HSPG2/Perlecan antibodies and DAPI and imaged with 25x objective on Leica SP8.

BMP4 induction assay

Primary interstitial cells were cultured in MEM α with 2% serum supplemented with factors indicated in triplicate and grown for 0, 12, 24, and 48 hrs at 37 °C in 5% CO_2. Cells were fixed at specified timepoints, stained for GATA3, PDGFRB, and DAPI and imaged with 25x objective on Leica SP8. Quantification of average protein intensity per cell was performed in Imaris on three fields. Cells were collected for RNA at specified timepoints, cDNA synthesized with Superscript IV VILO, and QCPR was performed on Viia 7 (Applied Biosystems) for *GAPDH* (Fwd-GGAGCGAGATCCCTCCAAAAT, Rev-GGCTGTTGTCATACTTCTCATGG), *ID1* (Fwd- CTGCTCTACGACATGAACGG, Rev-GAAGGTCCCTGATGTAGTCGAT) and *GATA3* (Fwd- GCCCCTCATTAAGCCCAA, Rev-TTGTGGTGGTCTGACAGTTCG). Delta Ct method was used to calculate fold change relative to 0 hr sample.

References

BROWN, A. C., MUTHUKRISHNAN, S. D. & OXBURGH, L. 2015. A synthetic niche for nephron progenitor cells. *Dev Cell,* 34**,** 229-41.

FINKENZELLER, G., HAGER, S. & STARK, G. B. 2012. Effects of bone morphogenetic protein 2 on human umbilical vein endothelial cells. *Microvasc Res,* 84**,** 81-5.

LAKE, B. B., AI, R., KAESER, G. E., SALATHIA, N. S., YUNG, Y. C., LIU, R., WILDBERG, A., GAO, D., FUNG, H. L., CHEN, S., VIJAYARAGHAVAN, R., WONG, J., CHEN, A., SHENG, X., KAPER, F., SHEN, R., RONAGHI, M., FAN, J. B., WANG, W., CHUN, J. & ZHANG, K. 2016. Neuronal subtypes and diversity revealed by single-nucleus RNA sequencing of the human brain. *Science,* 352**,** 1586-90.

LAKE, B. B., CHEN, S., SOS, B. C., FAN, J., KAESER, G. E., YUNG, Y. C., DUONG, T. E., GAO, D., CHUN, J., KHARCHENKO, P. V. & ZHANG, K. 2017. Integrative single-cell analysis of transcriptional and epigenetic states in the human adult brain. *Nat Biotechnol*.

TRAPNELL, C., CACCHIARELLI, D., GRIMSBY, J., POKHAREL, P., LI, S., MORSE, M., LENNON, N. J., LIVAK, K. J., MIKKELSEN, T. S. & RINN, J. L. 2014. The dynamics and regulators of cell fate decisions are revealed by pseudotemporal ordering of single cells. *Nat Biotechnol,* 32**,** 381-6.

WU, Y., TAMAYO, P. & ZHANG, K. 2018. Visualizing and Interpreting Single-Cell Gene Expression Datasets with Similarity Weighted Nonnegative Embedding. *Cell Syst,* 7**,** 656-666.e4.

YARROW, J. C., PERLMAN, Z. E., WESTWOOD, N. J. & MITCHISON, T. J. 2004. A high-throughput cell migration assay using scratch wound healing, a comparison of image-based readout methods. *BMC Biotechnol,* 4**,** 21.

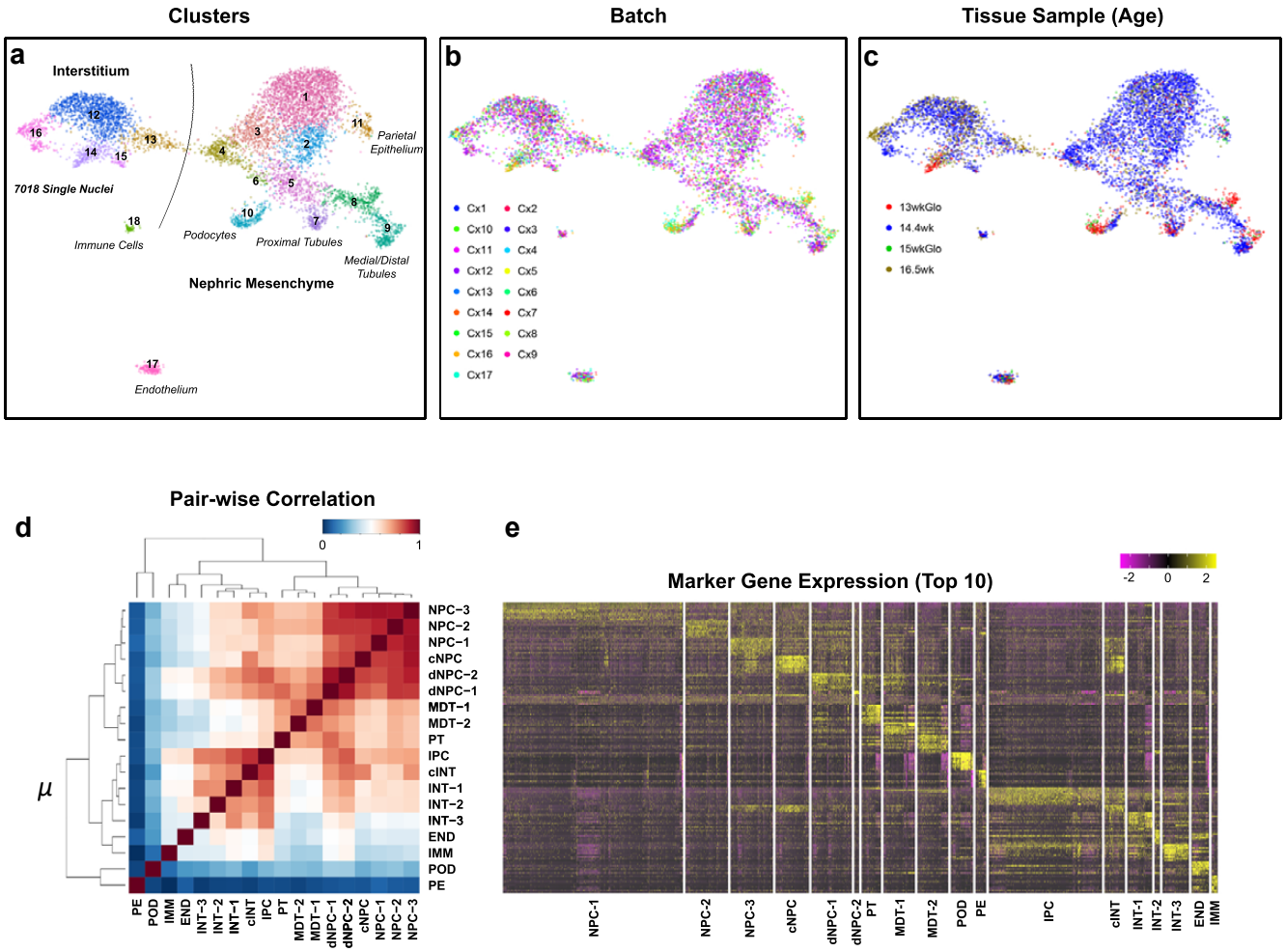

Fig. S1, related to Fig. 2. snDrop-seq data shows distinct cell-type specific clustering. (a) Uniform Manifold Approximation and Projection (UMAP) plot of cell type clusters as shown in Fig. 1a. **(b)** UMAP plot as in (a) showing experimental batch identities (**Table S1**). **(c)** UMAP plot as in (a) showing sample identities (**Table S1**). **(d)** Pairwise correlation plot showing Hierarchical clustering of r values (Pearson correlation coefficient) for all cell clusters shown in (a) and based on averaged expression values for genes differentially expressed between clusters (**Table S4**, adjusted p value < 0.05). **(e)** Heatmap of expression for the top 10 markers for each cluster based on average log fold change (**Table S4**).

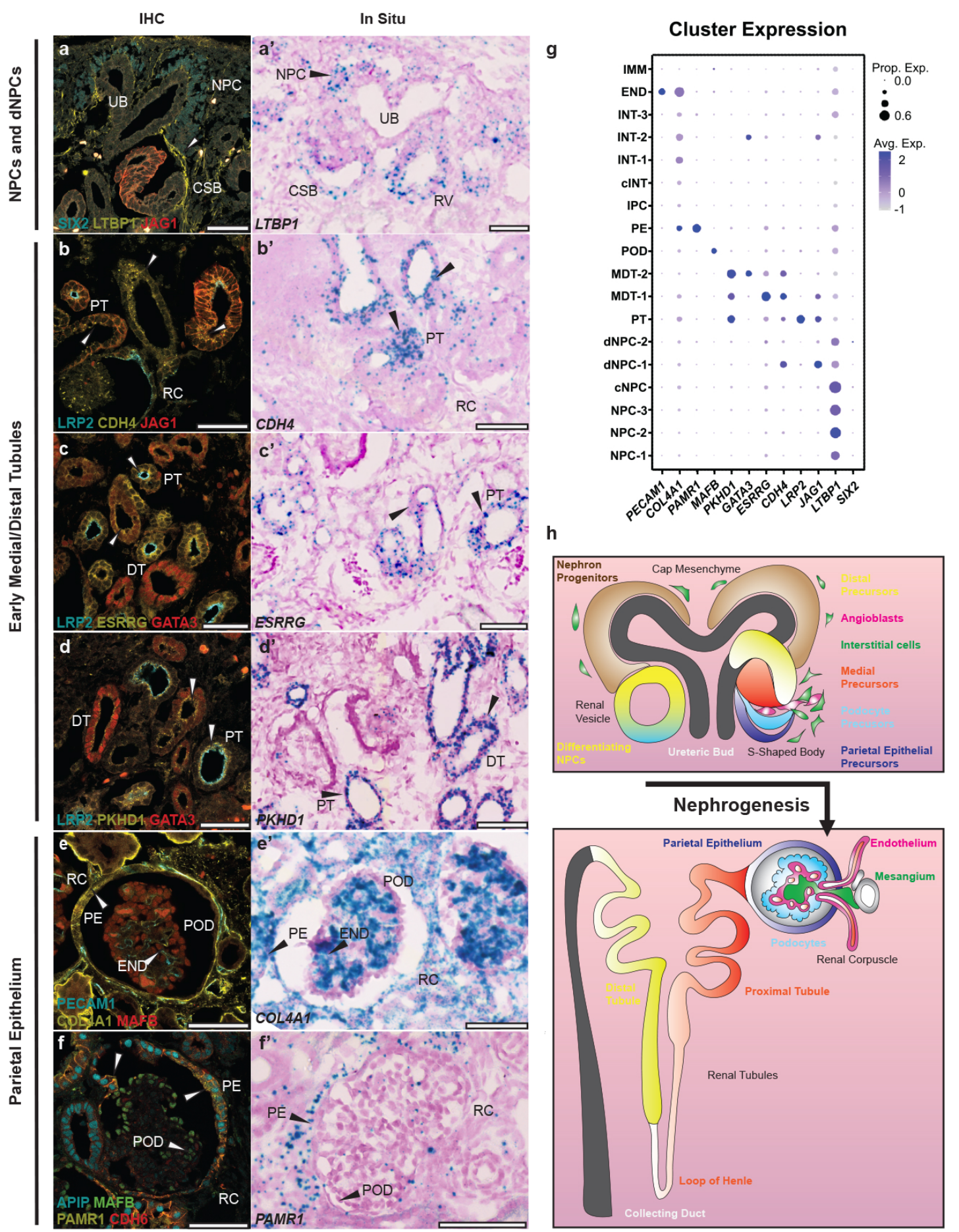

Fig. S2, related to Fig. 2. Validation of scRNA-identified cell population-enriched marker genes in human fetal kidney. (a-f) Immunofluorescent staining of nephrogenic lineage markers as specified in fields. **(a'-f')** RNAscope in situ hybridization of nephrogenic lineage markers as specified in fields. **(g)** Dot pots showing relative expression (blue color intensity) and relative number of positive nuclei (dot size) for select markers within clusters identified in **Fig. 1a. (h)** Schematic of nephrogenesis showing distinct stages and spatial localization of cell types in the cap mesenchyme, SSB, mature renal tubules and RCs.

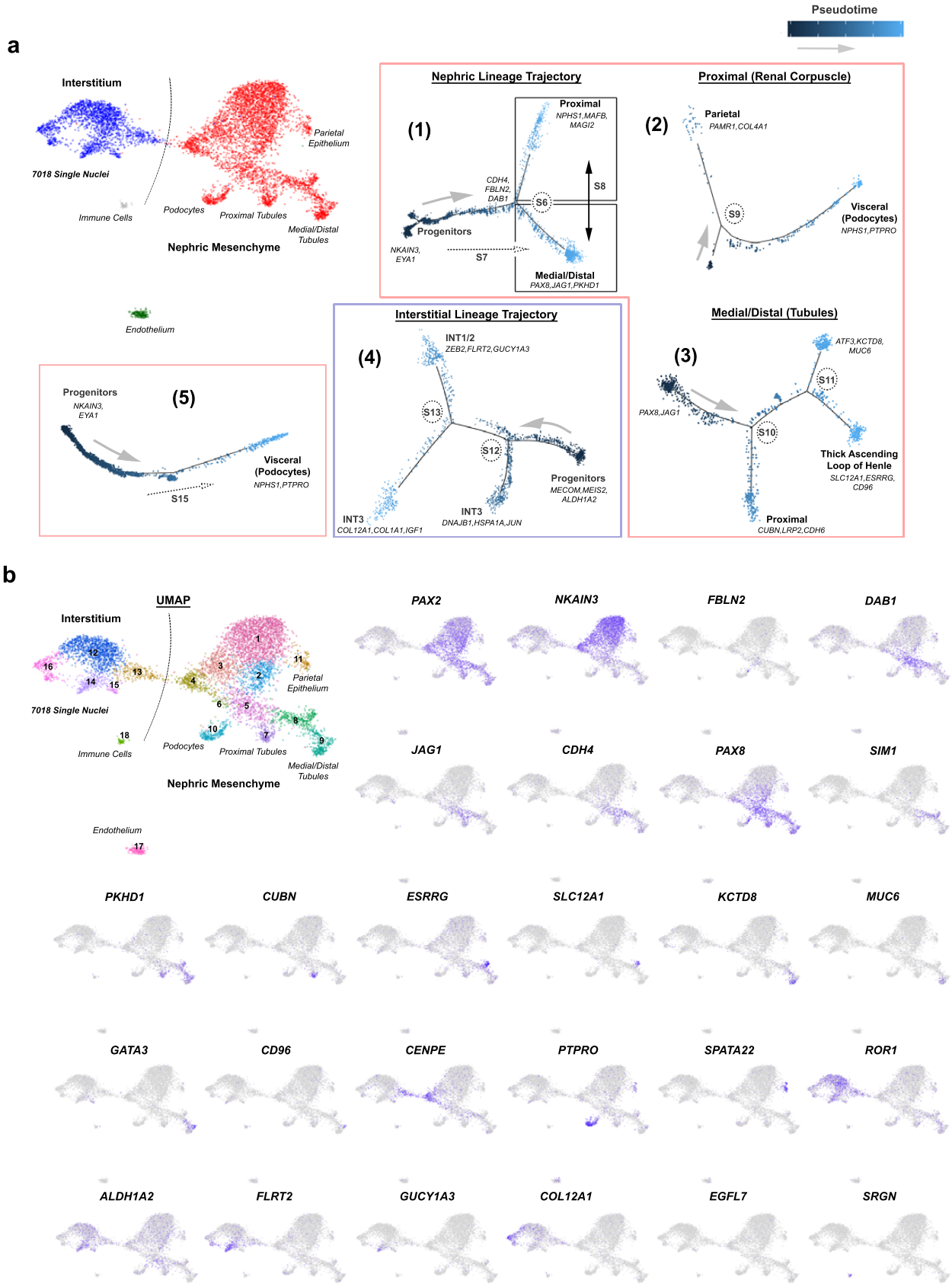

Fig. S3, related to Fig. 2. Developmental trajectory analyses. (a) UMAP plot as shown in **Fig. 1a** highlighting major cell populations (nephrogenic mesenchyme – red, interstitium, blue) used for pseudotemporal ordering using Monocle. Panels (1) to (5) represent five separate trajectories: (1) global nephrogenic mesenchyme trajectory; (2) proximal nephrogenic mesenchyme trajectory to generate parietal and visceral epithelial cell types of the RC; (3) medial/distal mesenchyme trajectory to give rise to the proximal, medial and distal tubules of the nephron; (4) interstitial lineage trajectory towards distinct INT-1/2 and INT-3 lineages; (5) progenitor trajectory to give rise to podocytes (see Methods). Supplementary tables for differentially expressed genes identified from branch-point (BEAM) analyses, global pseudotemporal analyses or that are differentially expressed between data sets occupying each branch are indicated (S6-S13, S15). Corresponding marker genes are indicated. **(b)** UMAP plots for all cell-type clusters (shown in top left) indicating expression level (gray = low, blue = high) of select marker genes.

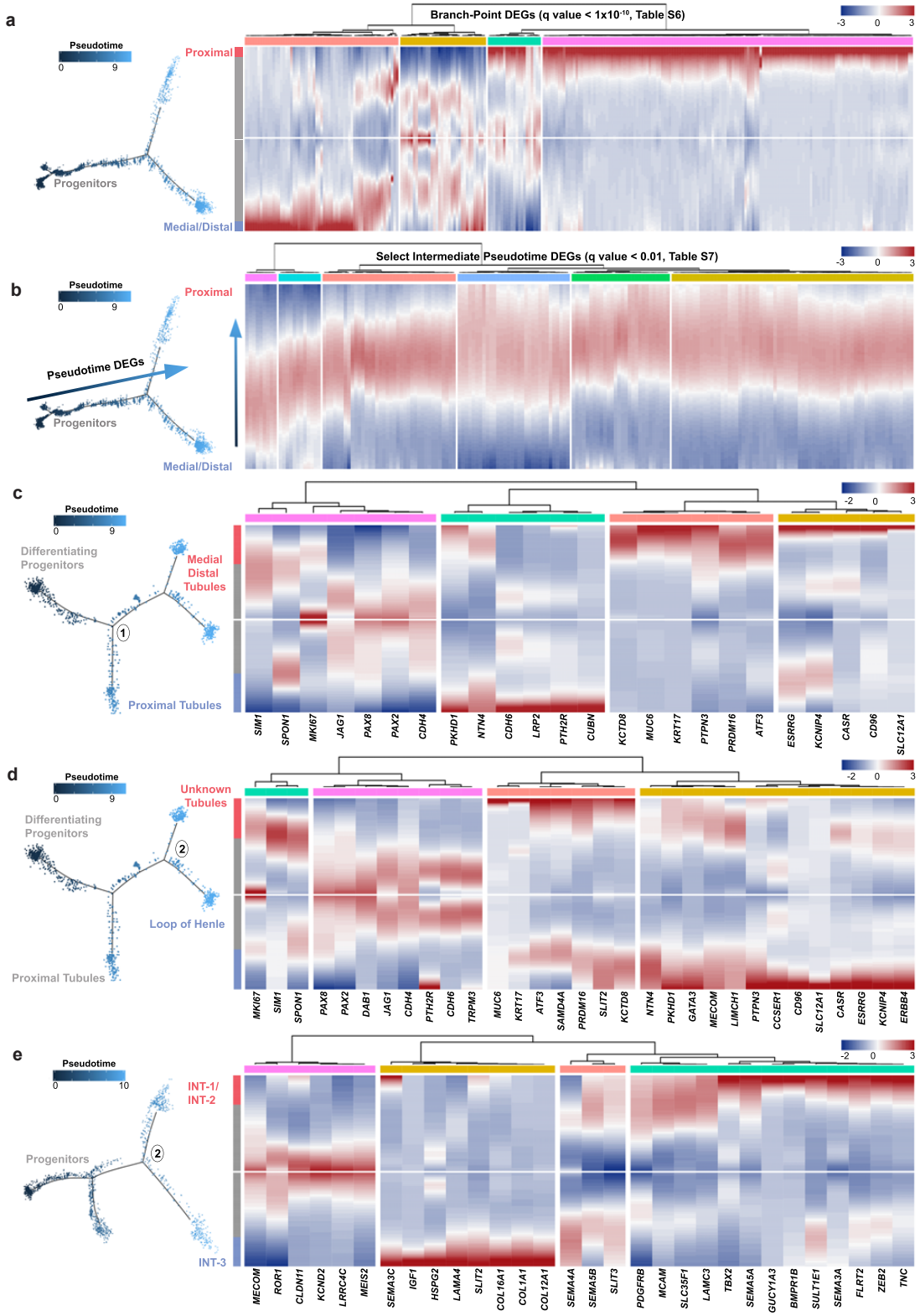

Fig. S4, related to Fig. 2. Trajectory expression analyses. (a) Differentially expressed genes (DEGs) were identified from the proximal and medial/distal mesenchymal branch-point (BEAM analysis, Monocle) of the global nephrogenic trajectory. Heatmap shows expression of DEGs with q value < $1x10^{-10}$ (**Table S6**) progressing from NPCs (center, gray) to proximal (red, top) or medial/distal (blue, bottom) mesenchyme. **(b)** Genes showing significant variation by pseudotime (q value < 0.01) were determined (Monocle) for the global nephrogenic trajectory (**Table S7**) and a heatmap for a subset showing intermediate pseudotime expression is shown (bottom = early, top = late). **(c)** Trajectory analysis of the medial/distal mesenchyme branch of **(a)**. DEGs for branch 1 were determined (BEAM analysis, Monocle, **Table S10**) and expression values for select markers are plotted in a heatmap progressing from differentiating NPCs (center, gray) towards medial/distal tubules (red, top) or proximal tubules (blue, bottom). **(d)** DEGs were determined as in **(c)** except with BEAM analysis on branch 2 (**Table S11**) and a heatmap for select marker genes showing expression progressing from differentiating NPCs (gray, center) towards medial tubules (red, top) or distal tubules (blue, bottom). **(e)** Trajectory analysis of interstitial lineages (reversal of plots shown in Supplemental Figures 2-3), showing differential expression analysis of branch 2 (BEAM analysis, Monocle, **Table S13**) and a heatmap for select markers showing expression progressing from IPCs (center, gray) towards either INT-1/2 (red, top) or INT-3 (blue, bottom).

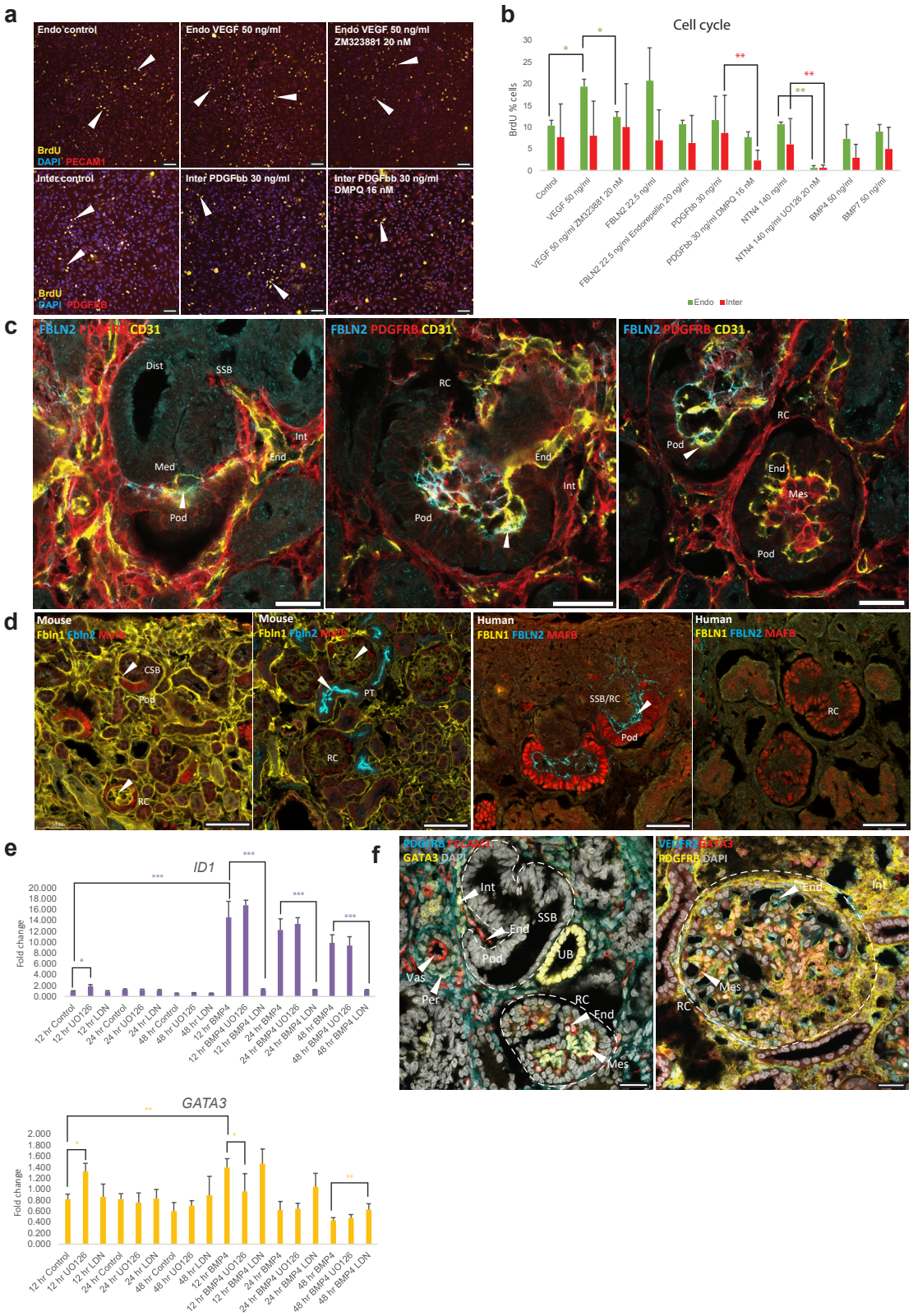

Fig. S5, related to Fig. 3-5. BMP4, NTN4, and FBLN2 effects in vitro and comparison of mouse and human kidney localization. (a) Representative images and **(b)** quantitation of BrdU incorporation in endothelial or interstitial cells in response to factors indicated (Scale bar= 100 μm). **(c)** Immunostaining of FBLN2, endothelial, and interstitial markers indicated in human fetal kidney section indicating contact points between FBLN2 and endothelium and podocytes. **(d)** Comparison of FBLN2 and FBLN1 localization in developing nephrons between E15.5 mouse and 16 wk human. **(e)** Relative expression of *ID1* or *GATA3* in cultured interstitial cells in response to 0 or 300 ng/ml of BMP4 with or without 20 nM U0126 or 200 μM LDN-193189. **(f)** Immunostaining of GATA3, endothelial, and interstitial markers indicated in HFKs in SShaped Bodies and early renal corpuscles, and late renal corpuscles (arrowheads). (Scale bars= 25 μm). Podocyte (Pod), Distal nephron (Dist), S-Shaped Body (SSB), Renal Corpuscle (RC), Endothelium (End) Interstitium (Int), Mesangium (Mes), Ureteric Bud (UB), Vasculature (Vas), Pericytes (Per). Data are represented as mean +/- SEM. One asterisk (*) indicates p value smaller than 0.05 ($p<0.05$). Two asterisks (**) indicate p value smaller than 0.01 ($p<0.01$) Three asterisks (***) indicate p value smaller than 0.001 ($p<0.001$).